

# **$^{231}\text{Pa}$ and $^{230}\text{Th}$ in the ocean model of the Community Earth System Model (CESM1.3)**

Sifan Gu<sup>1</sup>, Zhengyu Liu<sup>2</sup>

<sup>1</sup>Department of Atmospheric and Oceanic Sciences and Center for Climate Research,  
University of Wisconsin-Madison, Madison, WI, USA

<sup>2</sup>Atmospheric Science Program, Department of Geography, Ohio State University,  
Columbus, OH, USA

Correspondence to: Sifan Gu (sgu28@wisc.edu)

## **Abstract**

Sediment  $^{231}\text{Pa}/^{230}\text{Th}$  activity ratio is emerging as an important proxy for deep ocean circulation in the past. In order to allow for a direct model-data comparison and to improve our understanding of sediment  $^{231}\text{Pa}/^{230}\text{Th}$  activity ratio, we implement  $^{231}\text{Pa}$  and  $^{230}\text{Th}$  in the ocean component of the Community Earth System Model (CESM). In addition to the fully coupled implementation of the scavenging behavior of  $^{231}\text{Pa}$  and  $^{230}\text{Th}$  with the active marine ecosystem module (p-coupled), another form of  $^{231}\text{Pa}$  and  $^{230}\text{Th}$  have also been implemented with prescribed particle flux fields of the present climate (p-fixed). The comparison of the two forms of  $^{231}\text{Pa}$  and  $^{230}\text{Th}$  helps to isolate the influence of the particle fluxes from that of ocean circulation. Under present day climate forcing, our model is able to simulate water column  $^{231}\text{Pa}$  and  $^{230}\text{Th}$  activity and sediment  $^{231}\text{Pa}/^{230}\text{Th}$  activity ratio in good agreement with available observations. In addition, in response to freshwater forcing, the p-coupled and p-fixed sediment  $^{231}\text{Pa}/^{230}\text{Th}$  activity ratios behave similarly over large areas of low productivity on long timescale, but can differ substantially in some regions of high productivity and on short timescale, indicating the importance of biological productivity in addition to ocean transport. Therefore, our model provides a potentially powerful tool to help the interpretation of sediment  $^{231}\text{Pa}/^{230}\text{Th}$  reconstructions and to improve our understanding of past ocean circulation and climate changes.

## 1. Introduction

Sediment  $^{231}\text{Pa}/^{230}\text{Th}$  activity ratio has been one major proxy for ocean circulation in the past (e.g. Yu et al. 1996; McManus et al. 2004; Gherardi et al. 2009).  $^{231}\text{Pa}$  (32.5 ka half-life) and  $^{230}\text{Th}$  (75.2 ka half-life) are produced at a constant rate approximately uniformly in the ocean by the  $\alpha$  decay of  $^{235}\text{U}$  and  $^{234}\text{U}$ , respectively, with a production activity ratio of 0.093 (Henderson and Anderson, 2003). Water column  $^{231}\text{Pa}$  and  $^{230}\text{Th}$  are subject to particle scavenging and transport to sediments (Bacon and Anderson, 1982; Nozaki et al., 1987). Different scavenging efficiency results in different ocean residence time:  $^{231}\text{Pa}$  has a residence time of approximately 111 years and  $^{230}\text{Th}$  has a residence time of approximately 26 years (Yu et al., 1996). Longer residence time of  $^{231}\text{Pa}$  than  $^{230}\text{Th}$  makes  $^{231}\text{Pa}$  more subject to ocean transport and therefore in the modern ocean about 45% of  $^{231}\text{Pa}$  produced in the Atlantic is transported to the Southern Ocean (Yu et al., 1996), resulting a lower than 0.093 sediment  $^{231}\text{Pa}/^{230}\text{Th}$  activity ratio in the North Atlantic and higher than 0.093 sediment  $^{231}\text{Pa}/^{230}\text{Th}$  activity ratio in the Southern Ocean.

The application of the principle above to interpret sediment  $^{231}\text{Pa}/^{230}\text{Th}$  as the strength of Atlantic meridional overturning circulation (AMOC), however, can be complicated by other factors, leading to uncertainties in using  $^{231}\text{Pa}/^{230}\text{Th}$  as a proxy for past circulation (Keigwin and Boyle, 2008; Lippold et al., 2009; Scholten et al., 2008). In addition to the ocean transport, sediment  $^{231}\text{Pa}/^{230}\text{Th}$  is also influenced by particle flux and composition (Chase et al., 2002; Geibert and Usbeck, 2004; Scholten et al., 2008; Siddall et al., 2007; Walter et al., 1997). The region of a higher particle flux tends to have a higher  $^{231}\text{Pa}/^{230}\text{Th}$  (Kumar et al., 1993; Yong Lao et al., 1992), which is referred to as the “particle flux effect” (Siddall et al., 2005). Regional high particle flux in the water column will favor the removal of isotopes into the sediment, which leads to more isotopes transported into this region due to the down-gradient diffusive flux and subsequently more removal of isotopes into the sediment. Since  $^{231}\text{Pa}$  has a longer residence time, this effect is more prominent on  $^{231}\text{Pa}$  than on  $^{230}\text{Th}$  and therefore sediment  $^{231}\text{Pa}/^{230}\text{Th}$  will be higher in high productivity regions. Also, opal is able to scavenge  $^{231}\text{Pa}$  much more effectively than  $^{230}\text{Th}$ , leading to higher  $^{231}\text{Pa}/^{230}\text{Th}$  in high opal flux regions such as the Southern

Ocean (Chase et al., 2002). Moreover, sediment  $^{231}\text{Pa}/^{230}\text{Th}$  is suggested to record circulation change only within 1,000 m above the sediment, instead of the whole water column, complicating the interpretation of sediment  $^{231}\text{Pa}/^{230}\text{Th}$  reconstructions (Thomas et al., 2006). For example, sediment  $^{231}\text{Pa}/^{230}\text{Th}$  approaching 0.093 during Heinrich Stadial event 1(HS1) from the subtropical North Atlantic is interpreted as the collapse of AMOC (McManus et al., 2004). If sediment  $^{231}\text{Pa}/^{230}\text{Th}$  only records deepest water mass, it is possible that during HS1, AMOC shoals, as opposed to a fully collapse, yet an increase of deep water imported from the Southern Ocean featuring high  $^{231}\text{Pa}/^{230}\text{Th}$  can increase the sediment  $^{231}\text{Pa}/^{230}\text{Th}$  approaching the production ratio (0.093) (Thomas et al., 2006). Therefore, it is important to incorporate  $^{231}\text{Pa}$  and  $^{230}\text{Th}$  into climate models for a direct model-data comparison and to promote a thorough understanding of sediment  $^{231}\text{Pa}/^{230}\text{Th}$  as well as past ocean circulation.

$^{231}\text{Pa}$  and  $^{230}\text{Th}$  have been simulated in previous modeling studies (Dutay et al., 2009; Luo et al., 2010; Marchal et al., 2000; Rempfer et al., 2017; Siddall et al., 2005). Marchal et al., (2000) simulates  $^{231}\text{Pa}$  and  $^{230}\text{Th}$  in a zonally averaged circulation model, using the reversible scavenging model of Bacon and Anderson, (1982). One step further, Siddall et al. (2005) extends Marchal et al., (2000) by including particle dissolution with prescribed particle export production in a 3-D circulation model. Rempfer et al., (2017) further couples  $^{231}\text{Pa}$  and  $^{230}\text{Th}$  with active biogeochemical model and includes boundary scavenging and sediment resuspensions to improve model performance in simulating water column  $^{231}\text{Pa}$  and  $^{230}\text{Th}$  activity. Here we follow previous studies to implement  $^{231}\text{Pa}$  and  $^{230}\text{Th}$  into the Community Earth System Model (CESM). Our standard  $^{231}\text{Pa}$  and  $^{230}\text{Th}$  are coupled with active marine ecosystem model (“p-coupled”) and therefore is influenced by both ocean circulation change and particle flux change. To help to understand the influence of the particle flux, we have also implemented an auxiliary version of  $^{231}\text{Pa}$  and  $^{230}\text{Th}$  (“p-fixed”) for which the particle fluxes are fixed at prescribed values. Therefore, p-fixed  $^{231}\text{Pa}/^{230}\text{Th}$  is only influenced by ocean circulation change. By comparing the p-fixed  $^{231}\text{Pa}/^{230}\text{Th}$  with the p-coupled  $^{231}\text{Pa}/^{230}\text{Th}$ , we will be able to separate the effect of circulation change from particle flux change. In

addition, the p-fixed  $^{231}\text{Pa}$  and  $^{230}\text{Th}$  can be run without the marine ecosystem module, reducing computational cost by a factor of 3 in the ocean-alone model simulation, making it a computationally efficient tracer for sensitivity studies.

This paper describes the details of  $^{231}\text{Pa}$  and  $^{230}\text{Th}$  in CESM and serves as a reference for future studies using this tracer module. In section 2, we describe the model and the implementation of  $^{231}\text{Pa}$  and  $^{230}\text{Th}$ . In sections 3, we describe the experimental design. We will finally compare simulated  $^{231}\text{Pa}$  and  $^{230}\text{Th}$  fields with observations, show model sensitivities on model parameter and also sediment  $^{231}\text{Pa}/^{230}\text{Th}$  ratio response to freshwater forcing in Section 4.

## **2. Model Description**

### **2.1 Physical Ocean Model**

We implement  $^{231}\text{Pa}$  and  $^{230}\text{Th}$  in the ocean model (Parallel Ocean Program version 2, POP2) (Danabasoglu et al., 2012) of CESM (Hurrell et al., 2013). CESM is a state-of-the-art coupled climate model and studies describing model components and analyzing results can be found in a special collection in Journal of Climate (<http://journals.ametsoc.org/topic/ccsm4-cesm1>). We run the ocean-alone model, which is coupled to data atmosphere, land, ice and river runoff under the normal year forcing of CORE-II data (Large and Yeager, 2008), using the low-resolution version of POP2 with a nominal  $3^\circ$  horizontal resolution and 60 vertical layers.

### **2.2 Biogeochemical component (BGC)**

CESM has incorporated a marine ecosystem module that simulates biological variables (Moore et al., 2013). The marine ecosystem module has been validated against present day observations extensively (e.g. Doney et al., 2009; Long et al., 2013; Moore et al., 2002, 2004; Moore and Braucher, 2008). The implementation of  $^{231}\text{Pa}$  and  $^{230}\text{Th}$  requires particle fields:  $\text{CaCO}_3$ , opal and particulate organic carbon (POC). These particle fields can be obtained through the ecosystem driver from the ecosystem module (Jahn et al., 2015). The ecosystem module simulates the particle fluxes in reasonable agreement with the present-day observations. The pattern and magnitude of the annual mean particle fluxes ( $\text{CaCO}_3$ , opal, POC) leaving the



euphotic zone at 105m are similar to the satellite observations (Fig. 7.2.5 and 9.2.2 in Sarmiento and Gruber 2006) (Fig. 1 a~c): particle fluxes are higher in the high productivity regions such as high latitudes and equatorial Pacific; opal flux is high in the Southern Ocean. The remineralization scheme of particle is based on the ballast model of Armstrong et al., (2002). Detailed parameterizations for particle remineralization are documented in Moore et al., (2004) with temperature dependent remineralization length scales for POC and opal. We do not consider dust because it is suggested to be unimportant for  $^{231}\text{Pa}$  and  $^{230}\text{Th}$  fractionation (Chase et al., 2002; Siddall et al., 2005).

### 2.3 $^{231}\text{Pa}$ and $^{230}\text{Th}$ implementation

$^{231}\text{Pa}$  and  $^{230}\text{Th}$  are produced from the  $\alpha$  decay of  $^{235}\text{U}$  and  $^{234}\text{U}$  uniformly everywhere at constant rate  $\beta^i$  ( $\beta^{\text{Pa}} = 2.33 \cdot 10^{-3} \text{ dpm m}^{-3} \text{ yr}^{-1}$ ,  $\beta^{\text{Th}} = 2.52 \cdot 10^{-2} \text{ dpm m}^{-3} \text{ yr}^{-1}$ ).  $^{231}\text{Pa}$  and  $^{230}\text{Th}$  are also subjective to radioactive decay with the decay constant of  $\lambda^i$  ( $\lambda^{\text{Pa}} = 2.13 \cdot 10^{-5} \text{ yr}^{-1}$ ,  $\lambda^{\text{Th}} = 9.22 \cdot 10^{-6} \text{ yr}^{-1}$ ).

Another important process contributes to  $^{231}\text{Pa}$  and  $^{230}\text{Th}$  activity is the reversible scavenging by sinking particles (Bacon and Anderson, 1982), which describes the adsorption of isotopes onto sinking particles and desorption after the dissolution of particles. This process transports  $^{231}\text{Pa}$  and  $^{230}\text{Th}$  downward and leads to a general increase of  $^{231}\text{Pa}$  and  $^{230}\text{Th}$  activity with depth. The reversible scavenging considers total isotope activity ( $A_t^i$ ) as two categories (Eq. (1)): dissolved isotopes ( $A_d^i$ ) and particulate isotopes ( $A_p^i$ ) (superscript i refers to  $^{231}\text{Pa}$  and  $^{230}\text{Th}$ ) and  $A_p^i$  is the sum of the isotopes associated with different particle types ( $A_{j,p}^i$ ) (subscript j refers to different particle types:  $\text{CaCO}_3$ , opal and POC):

$$A_t^i = A_d^i + A_p^i = A_d^i + \sum_j A_{j,p}^i \quad (1)$$

Dissolved and particulate isotopes are assumed to be in equilibrium, which is a reasonable assumption in the open ocean (Bacon and Anderson, 1982; Henderson et

al., 1999; Moore and Hunter, 1985). The ratio between the particulate isotope activity and the dissolved isotope activity is set by a partition coefficient, K (Eq. (2)):

$$K_j^i = \frac{A_{j,p}^i}{A_d^i \cdot R_j} \quad (2)$$

, where  $R_j$  is the ratio of particle concentration ( $C_j$ ) to the density of seawater ( $1024.5 \text{ kg m}^{-3}$ ). Subscript j refers to different particle types ( $\text{CaCO}_3$ , opal and POC). Values of partition coefficient K used in our control simulation follows Chase et al., 2002 and Siddall et al., 2005 (Table 2).

Particulate isotopes ( $A_p^i$ ) will be transported by sinking particles, which is described by  $w_s \frac{\partial A_p^i}{\partial z}$  (Eq. (3)), where  $w_s$  is the sinking velocity. We don't differentiate between slow sinking small particles and rapid sinking large particles as in Dutay et al., (2009) and consider all particles as slowly sinking small particles with sinking velocity of  $w_s = 1000 \text{ m yr}^{-1}$  (Arsouze et al., 2009; Dutay et al., 2009; Kriest, 2002), which is similar to Rempfer et al., (2017) and Siddall et al., (2005). Any particulate isotopes ( $A_p^i$ ) at the ocean bottom layer are removed from the ocean as sediment, which is the sink for the isotope budget. Detailed vertical differentiation scheme to calculate this term in the model is provided in the supplementary material. The reversible scavenging scheme applied here is the same as the neodymium implementation in POP2 (Gu et al., 2017).

Therefore, the conservation equation for  $^{231}\text{Pa}$  and  $^{230}\text{Th}$  activity can be written as

$$\frac{\partial A_t^i}{\partial t} = \beta^i - \lambda^i A_t^i - w_s \frac{\partial A_p^i}{\partial z} + \text{Transport} \quad (3),$$

where the total isotope activity is controlled by decay from U (first term), radioactive decay (second term), reversible scavenging (third term) and physical transport by the ocean model (fourth term, including advection, convection and diffusion).  $A_p^i$  can be calculated by combining Eq. (1) and Eq. (2):

$$A_t^i = A_d^i + A_d^i \cdot (K_{POC}^i \cdot R_{POC} + K_{CaCO_3}^i \cdot R_{CaCO_3} + K_{opal}^i \cdot R_{opal})$$

$$= A_d^i \cdot (1 + K_{POC}^i \cdot R_{POC} + K_{CaCO_3}^i \cdot R_{CaCO_3} + K_{opal}^i \cdot R_{opal}), \quad (4)$$

which leads to

$$A_d^i = \frac{A_t^i}{1 + K_{POC}^i \cdot R_{POC} + K_{CaCO_3}^i \cdot R_{CaCO_3} + K_{opal}^i \cdot R_{opal}}, \quad (5)$$

put this back to Eq. (1), we get

$$A_p^i = A_t^i \cdot \left(1 - \frac{1}{1 + K_{POC}^i \cdot R_{POC} + K_{CaCO_3}^i \cdot R_{CaCO_3} + K_{opal}^i \cdot R_{opal}}\right) \quad (6)$$

Particle fields used in the reversible scavenging can be either prescribed or simultaneously generated from the marine ecosystem module. Therefore, two forms of  $^{231}\text{Pa}$  and  $^{230}\text{Th}$  are implemented in POP2: “p-fixed” and “p-coupled”. P-fixed  $^{231}\text{Pa}$  and  $^{230}\text{Th}$  use particle fluxes prescribed as annual mean particle fluxes generated from the marine ecosystem module under present day climate forcing (Fig.1). P-coupled  $^{231}\text{Pa}$  and  $^{230}\text{Th}$  use particle fluxes computed simultaneously from the marine ecosystem module. P-fixed and p-coupled  $^{231}\text{Pa}$  and  $^{230}\text{Th}$  can be turned on at the case build time and the p-coupled  $^{231}\text{Pa}$  and  $^{230}\text{Th}$  requires the ecosystem module to be turned on at the same time.

Comparing with previous studies of modeling  $^{231}\text{Pa}$  and  $^{230}\text{Th}$ , our p-fixed version is the same as Siddall et al., (2002), except that different prescribed particle fluxes are used. The p-coupled version allows coupling to biogeochemical module, which is similar to Rempfer et al., (2017), but we do not include boundary scavenging and sediment resuspensions as in Rempfer et al., (2017) because boundary scavenging and sediment resuspensions are suggested to be unimportant to influence the relationship between  $^{231}\text{Pa}_p/^{230}\text{Th}_p$  and AMOC strength (Rempfer et al., 2017).

### 3. Experiments

We run a control experiment (CTRL) and two experiments with different partition coefficients to show model sensitivity. We have both p-fixed and p-coupled  $^{231}\text{Pa}$  and  $^{230}\text{Th}$  in CTRL, but only p-fixed  $^{231}\text{Pa}$  and  $^{230}\text{Th}$  in sensitivity experiments. Equilibrium partition coefficients for  $^{231}\text{Pa}$  and  $^{230}\text{Th}$  vary among different particle types and the magnitude of the partition coefficients for different particle types remains uncertain (Chase et al., 2002; Chase and Robert F, 2004; Luo and Ku, 1999). Since the control experiment in Siddall et al., (2005) is able to simulate major features of  $^{231}\text{Pa}$  and  $^{230}\text{Th}$  distributions, we use the partition coefficients from the control experiment in Siddall et al., (2005) in our CTRL (Table 2). Two sensitivity experiments are performed with decreased (EXP\_1) and increased (EXP\_2) partition coefficients by a factor of 5 (Table 2).

All the experiments are ocean-alone experiments with the normal year forcing by CORE-II data (Large and Yeager, 2008). The  $^{231}\text{Pa}$  and  $^{230}\text{Th}$  activities are initiated from 0 in CTRL and are integrated for 2,000 model years until equilibrium is reached. EXP\_1 and EXP\_2 are initiated from 1,400 model year in CTRL and are integrated for another 800 model years to reach equilibrium.

Since sediment  $^{231}\text{Pa}/^{230}\text{Th}$  in North Atlantic has been used to reflect the strength of AMOC, to test how sediment  $^{231}\text{Pa}/^{230}\text{Th}$  in our model responds to the change of AMOC and the change of particle fluxes, we carried out a fresh water perturbation experiment (HOSING) with both p-fixed and p-coupled  $^{231}\text{Pa}$  and  $^{230}\text{Th}$ . Starting from 2,000 model year of CTRL, a freshwater flux of 1 Sv is imposed over the North Atlantic region of  $50^\circ\text{N}\sim 70^\circ\text{N}$  and the experiment is integrated for 1400 model years until both p-fixed and p-coupled sediment  $^{231}\text{Pa}/^{230}\text{Th}$  ratio have reached quasi-equilibrium. The partition coefficients used in HOSING are the same as in CTRL.

## 4. Results

### 4.1 Control Experiment

P-fixed and p-coupled version of  $^{231}\text{Pa}$  and  $^{230}\text{Th}$  in CTRL show identical results (Fig. 2-4). P-fixed and p-coupled dissolved and particulate  $^{231}\text{Pa}$  and  $^{230}\text{Th}$  in CTRL are highly correlated with each other with correlations greater than 0.995 and

regression coefficients are all near 1.0 ( $R^2 > 0.995$ ). The correlation coefficient between p-fixed and p-coupled sediment  $^{231}\text{Pa}/^{230}\text{Th}$  activity ratios in CTRL is 0.99 and the regression coefficient is 0.9 ( $R^2 = 0.98$ ). This is expected because the particle fields used in p-fixed version are prescribed as the climatology of the particle fields used in the p-coupled version. Therefore, under the same climate forcing, p-fixed and p-coupled version of  $^{231}\text{Pa}$  and  $^{230}\text{Th}$  should be very similar. For the discussion of results in CTRL below, we only discuss the p-fixed  $^{231}\text{Pa}$  and  $^{230}\text{Th}$ .

The residence time of both  $^{231}\text{Pa}$  and  $^{230}\text{Th}$  in CTRL are comparable with observations. The residence time is calculated as the ratio of global average total isotope activity and the radioactive ingrowth of the isotope. Residence time in CTRL is 118 yr for  $^{231}\text{Pa}$  and 33 yr for  $^{230}\text{Th}$  (Table 2), which are of the same magnitude as 111 yr for  $^{231}\text{Pa}$  and 26 yr for  $^{230}\text{Th}$  in observation (Yu et al., 1996).

CTRL can simulate the general features of dissolved water column  $^{231}\text{Pa}$  and  $^{230}\text{Th}$  activities. Dissolved  $^{231}\text{Pa}$  and  $^{230}\text{Th}$  activities increase with depth in CTRL, as shown in two GEOTRACES transects (Deng et al., 2014; Hayes et al., 2015) in the Atlantic (Fig. 2 and 3). The dissolved  $^{231}\text{Pa}$  and  $^{230}\text{Th}$  activities in CTRL are also at the same order of magnitude as in observations in the most of the ocean, except that simulated values are larger than observations in the abyssal, which is also the case in Siddall et al., (2005) and Rempfer et al., (2017) (their Fig. 2 and 3, experiment Re3d). Our model is unable to simulate the realistic dissolved  $^{231}\text{Pa}$  and  $^{230}\text{Th}$  activities in the abyssal probably because boundary scavenging and sediment resuspensions are not included in our model. In Rempfer et al., 2017, without boundary scavenging and sediment resuspension, dissolved  $^{231}\text{Pa}$  and  $^{230}\text{Th}$  activities are quite large in the deep ocean. However, if boundary scavenging and sediment resuspension are included, the water column dissolved  $^{231}\text{Pa}$  and  $^{230}\text{Th}$  activity is in the right magnitude compared with observation. Therefore, we hypothesize that with boundary scavenging and sediment resuspensions added, dissolved  $^{231}\text{Pa}$  and  $^{230}\text{Th}$  activities in the abyssal should be greatly reduced.

A more quantitative model-data comparison is shown in Fig. 5. The linear regression coefficient between model results and observations (references of observations are listed in Table 3), an indication of model ability to simulate  $^{231}\text{Pa}$

and  $^{230}\text{Th}$  activity (Dutay et al., 2009), is near 1.0 for dissolved  $^{231}\text{Pa}$  and  $^{230}\text{Th}$  (1.02 for  $[\text{}^{231}\text{Pa}]_d$  and 1.14 for  $[\text{}^{230}\text{Th}]_d$ ), suggesting that CTRL can simulate the dissolved  $^{231}\text{Pa}$  and  $^{230}\text{Th}$  in good agreement with observations. However, the simulation of the particulate activity is not as good as the dissolved activity. Particulate activity is overall larger than observation in the surface ocean and smaller than observation in the deep ocean for both particulate  $^{231}\text{Pa}$  and  $^{230}\text{Th}$ . The regression coefficient for particulate  $^{231}\text{Pa}$  and  $^{230}\text{Th}$  is 0.02 for  $[\text{}^{231}\text{Pa}]_p$  and 0.05 for  $[\text{}^{230}\text{Th}]_p$ . The poor performance in simulating water column particulate  $^{231}\text{Pa}$  and  $^{230}\text{Th}$  activities is also in previous modeling studies (Dutay et al., 2009; Siddall et al., 2005), because of similar modelling scheme applied. However, the simulated  $^{231}\text{Pa}_p/^{230}\text{Th}_p$  is in reasonable agreement with observations. The  $^{231}\text{Pa}_p/^{230}\text{Th}_p$  along two GEOTRACES transects (Fig. 2 and 3) show the similar pattern and magnitude as in Rempfer et al., (2017), consistent with observations. Decrease of  $^{231}\text{Pa}_p/^{230}\text{Th}_p$  with depth is well simulated, which is suggested to be caused by the lateral transport of  $^{231}\text{Pa}$  from North Atlantic to Southern Ocean by AMOC (Gherardi et al., 2009; Lippold et al., 2011, 2012a; Luo et al., 2010; Rempfer et al., 2017).

The sediment  $^{231}\text{Pa}/^{230}\text{Th}$  in CTRL is overall consistent with observations (references of observations are listed in Table 3). The North Atlantic shows low sediment  $^{231}\text{Pa}/^{230}\text{Th}$  activity ratio as in observations because  $^{231}\text{Pa}$  is more subject to the southward transport by active ocean circulation than  $^{230}\text{Th}$  because of its longer residence time. The Southern Ocean maximum in the sediment  $^{231}\text{Pa}/^{230}\text{Th}$  activity ratio is also simulated in CTRL. High opal fluxes in the Southern Ocean, which preferentially removes  $^{231}\text{Pa}$  into sediment ( $K_{opal}^{231Pa} > K_{opal}^{230Th}$ ) (Chase et al., 2002), leading to increased sediment  $^{231}\text{Pa}/^{230}\text{Th}$  activity ratio. In addition, upwelling in the Southern Ocean brings up deep water enriched with  $^{231}\text{Pa}$ , which is transported from the North Atlantic, to shallower depth and further contribute to the scavenging. CTRL can also produce higher sediment  $^{231}\text{Pa}/^{230}\text{Th}$  activity ratio in regions with high particle production (e.g. the Eastern equatorial Pacific, the North Pacific and the Indian Ocean) due to the “particle flux effect”. Specifically, in North Atlantic, the distribution of sediment  $^{231}\text{Pa}/^{230}\text{Th}$  matches the distribution of

particle, especially opal, production: sediment  $^{231}\text{Pa}/^{230}\text{Th}$  is higher where opal production is high, and vice versa (Fig. 4 and Fig. 1c). Quantitatively, the regression coefficient between sediment  $^{231}\text{Pa}/^{230}\text{Th}$  in CTRL and observation in the Atlantic is 0.86, which is larger than in other basins. This suggests that sediment  $^{231}\text{Pa}/^{230}\text{Th}$  is better simulated in the Atlantic than in other basins. One possible explanation is that sediment  $^{231}\text{Pa}/^{230}\text{Th}$  in the Atlantic is controlled by both ocean circulation and particle flux, while in other basins sediment  $^{231}\text{Pa}/^{230}\text{Th}$  is controlled almost only by particle flux. With active AMOC, the north south gradient of sediment  $^{231}\text{Pa}/^{230}\text{Th}$  can be simulated. However, for example, in the Southern Ocean, sediment  $^{231}\text{Pa}/^{230}\text{Th}$  is dominantly controlled by opal flux, which varies on small scales and is difficult for simulation. Therefore, model performance in simulating sediment  $^{231}\text{Pa}/^{230}\text{Th}$  in the Southern Ocean is not as good as in the Atlantic.

#### 4.2 Sensitivity on partition coefficient K

In this section, we show model sensitivity on partition coefficient by increasing and decreasing the partition coefficient, K, by a factor of 5, but keeping the relative ratio for different particles the same (Table 2). Our model shows similar model sensitivity as in Siddall et al., (2005) as discussed below.

As stated in Siddall et al., (2005), the isotope decay term in Eq. (3) is three orders of magnitude less than the production term. If we neglect the transport term and the decay term in Eq. (3) and assume particulate phase activity at the surface as 0, when reach equilibrium, the activity of particulate phase will be as in Eq. (7). Eq. (7) combined with Eq. (2) and  $R_i = \frac{F}{w_s * \rho}$ , we can obtain Eq. (8). Under the assumption that there is isotope decay and ocean transport, Eq. (7) suggests that the particulate isotope activity depends on the production rate and settling velocity and will increase linearly with depth. Eq. (8) suggests that the dissolved isotope activity depends on the production rate, partition coefficient K and particle flux and will also increase linearly with depth. Any departure from this linear relationship with depth is due to ocean transport, which is suggested by observations (Bacon and Anderson,

1982; Roy-Barman et al., 1996). Results of Eq. (7) and Eq. (8) can help to understand the differences in Exp\_1 and Exp\_2.

Increasing K will decrease water column dissolved  $^{231}\text{Pa}$  and  $^{230}\text{Th}$  activities but won't change particulate  $^{231}\text{Pa}$  and  $^{230}\text{Th}$  too much (Fig. 6). Magnitude of dissolved  $^{231}\text{Pa}$  and  $^{230}\text{Th}$  in Exp\_1 (smaller K) is at least one order larger than that in Exp\_2 (larger K), while magnitude of particulate  $^{231}\text{Pa}$  and  $^{230}\text{Th}$  in Exp\_1 and Exp\_2 is in the same order. As suggested by Eq. (8), if there is no isotope decay and no ocean transport, larger K will lead to smaller dissolved isotope activity but unchanged particulate activity. Intuitively, larger K will lead to more  $^{231}\text{Pa}$  and  $^{230}\text{Th}$  attached to particles and further buried into sediment, which increases the sink for the  $^{231}\text{Pa}$  and  $^{230}\text{Th}$  budget. With the sources for  $^{231}\text{Pa}$  and  $^{230}\text{Th}$  staying the same, dissolved  $^{231}\text{Pa}$  and  $^{230}\text{Th}$  will be reduced. Increasing K will also reduce the vertical gradient of dissolved  $^{231}\text{Pa}$  and  $^{230}\text{Th}$  as reversible scavenging act as the vertical transport and increase this vertical transport can decrease the vertical gradient. However, changes in the particulate  $^{231}\text{Pa}$  and  $^{230}\text{Th}$  is relatively small (Fig. 6). Eq. (7) suggests that particulate phase activity it is independent of K. Therefore, changing K will have limited influence on particulate phase activity.

$$A_p^i(z) = \frac{\beta^i}{w_s} \cdot z \quad (7)$$

$$A_d^i(z) = \frac{\rho\beta^i}{K^i F} \cdot z \quad (8)$$

Increasing K will also reduce the spatial gradient in sediment  $^{231}\text{Pa}/^{230}\text{Th}$  activity ratio and vice versa (Fig. 7). Larger K will decrease the  $^{231}\text{Pa}$  and  $^{230}\text{Th}$  residence time and most isotopes produced in the water column are removed into sediment locally (Table 2). Therefore, sediment  $^{231}\text{Pa}/^{230}\text{Th}$  ratio becomes more homogeneous and approaching the production ration of 0.093 (Fig. 7b). The deviation (the root mean squared error) of sediment  $^{231}\text{Pa}/^{230}\text{Th}$  is 0.0726 in CTRL, 0.0770 in Exp\_1 and 0.0739 in Exp\_2. The linear regression coefficients between sediment  $^{231}\text{Pa}/^{230}\text{Th}$  in the model and the observations are listed in Table S1 in the



supplementary information. Although the performance of global sediment  $^{231}\text{Pa}/^{230}\text{Th}$  in Exp\_1 is better than CTRL, the performance of Atlantic  $^{231}\text{Pa}/^{230}\text{Th}$  in Exp\_1 is worse. We consider better simulating sediment  $^{231}\text{Pa}/^{230}\text{Th}$  in the Atlantic is more important since the most important application of sediment  $^{231}\text{Pa}/^{230}\text{Th}$  is using sediment  $^{231}\text{Pa}/^{230}\text{Th}$  in the North Atlantic to reconstruct past AMOC. In addition, water column isotope activity is too large in Exp\_1 compared with observation. Therefore, the partition coefficient in CTRL is of the right order of magnitude.

#### 4.3. Sediment $^{231}\text{Pa}/^{230}\text{Th}$ ratio in HOSING

Potential changes in the export of biogenic particles makes using  $^{231}\text{Pa}/^{230}\text{Th}$  ratio to reconstruct AMOC strength under debate. In response to freshwater perturbation in the North Atlantic, both biological productivity and AMOC strength will change and will influence sediment  $^{231}\text{Pa}/^{230}\text{Th}$  in different ways. Our model with p-fixed and p-coupled  $^{231}\text{Pa}$  and  $^{230}\text{Th}$  can help to detangle these two effects. In this section, we examine the sediment  $^{231}\text{Pa}/^{230}\text{Th}$  (p-fixed and p-coupled) response in the North Atlantic to idealized fresh water perturbation.

In HOSING, after applying freshwater forcing to the North Atlantic, AMOC strength quickly decreases to a minimum of 2 Sv (AMOC\_off) (Fig. 9a). During the AMOC\_off state, compared with CTRL with active AMOC (AMOC\_on), p-fixed sediment  $^{231}\text{Pa}/^{230}\text{Th}$  shows an overall increase in the North Atlantic and a decrease in the South Atlantic (Fig. 10b) because of the reduced southward transport of  $^{231}\text{Pa}$  from the North Atlantic by AMOC, consistent with paleo proxy evidence there (e.g. Gherardi et al., 2005, 2009; McManus et al., 2004). The overall increase of sediment  $^{231}\text{Pa}/^{230}\text{Th}$  ratio in the North Atlantic in response to the AMOC collapse can be seen more clearly in the time evolution of the sediment  $^{231}\text{Pa}/^{230}\text{Th}$  ratio averaged from 20°N to 60°N in the North Atlantic (Fig.9b, green). Quantitatively, the  $^{231}\text{Pa}/^{230}\text{Th}$  increases from 0.074 in AMOC\_on to 0.098 in AMOC\_off in the p-fixed version, approaching the production ratio of 0.093. This increase of  $^{231}\text{Pa}/^{230}\text{Th}$  is also in the subtropical North Atlantic from the two sites near Bermuda Rise (Fig. 9e and f), which is of comparable magnitude with the change from LGM to HS1 in

reconstructions there (McManus et al., 2004). In addition, the pattern of p-fixed (Fig.10a) sediment  $^{231}\text{Pa}/^{230}\text{Th}$  ratio during the Atlantic in AMOC\_off state is similar to the opal distribution (Fig.1b) because, without active circulation, sediment  $^{231}\text{Pa}/^{230}\text{Th}$  ratio is more controlled by particle flux effect, which is similar to the Pacific in CTRL. It is further noted that our p-fixed sediment  $^{231}\text{Pa}/^{230}\text{Th}$  ratio in HOSING behaves similarly to that in Siddall et al., (2007).

The overall increase in p-fixed sediment  $^{231}\text{Pa}/^{230}\text{Th}$  ratio in the North Atlantic is not homogenous and the magnitude of the change between AMOC\_on and AMOC\_off varies with location depending on the distribution of particle flux, especially the opal flux (Fig.9 and 10). The maximum increase in p-fixed sediment  $^{231}\text{Pa}/^{230}\text{Th}$  ratio occurs near 40°N western Atlantic (Fig. 10a), where the opal production in our model is maximum in North Atlantic (Fig. 1b). The sediment  $^{231}\text{Pa}/^{230}\text{Th}$  ratio in this region during AMOC\_on is larger than production ratio of 0.093 because opal maximum provides extra  $^{231}\text{Pa}$  to this region (“particle flux effect”), which overwhelms the active ocean circulation transporting  $^{231}\text{Pa}$  southward outside this region (Fig. 9d, green). During AMOC\_off, without active ocean circulation, the particle flux effect becomes even stronger because less  $^{231}\text{Pa}$  is transported out of the North Atlantic and p-fixed sediment  $^{231}\text{Pa}/^{230}\text{Th}$  ratio becomes even larger. It should be noted that the opal maximum in this region is not in the observation (Fig. 7.2.5 in Sarmiento and Gruber 2006). However, our sediment  $^{231}\text{Pa}/^{230}\text{Th}$  response in HOSING is self-consistent with the particle flux in our model since the location of maximum  $^{231}\text{Pa}/^{230}\text{Th}$  increase matches the location of opal flux in our model.

In most regions of the Atlantic, p-coupled sediment  $^{231}\text{Pa}/^{230}\text{Th}$  shows a similar response to p-fixed  $^{231}\text{Pa}/^{230}\text{Th}$  in HOSING. The evolution of p-fixed and p-coupled sediment  $^{231}\text{Pa}/^{230}\text{Th}$  activity ratio in HOSING are highly correlated (Fig. 11a). The change of sediment  $^{231}\text{Pa}/^{230}\text{Th}$  ratio from AMOC\_on to AMOC\_off are similar in both the p-fixed and p-coupled version (Fig.11b). The correlation between p-fixed and p-coupled sediment  $^{231}\text{Pa}/^{230}\text{Th}$  ratio change from AMOC\_on to AMOC\_off is 0.72 (1455points) and the linear regression coefficient is 0.71 ( $R^2 = 0.52$ ). A high correlation between p-fixed and p-coupled response mainly happens

over low productivity regions (Fig.1, 10, and 11), where circulation effect on sediment  $^{231}\text{Pa}/^{230}\text{Th}$  is more important than the particle flux change in HOSING.

In spite of these similarities discussed above, the responses of p-fixed and p-coupled sediment  $^{231}\text{Pa}/^{230}\text{Th}$  to the fresh water forcing can differ significantly in high productivity regions because of the productivity change. With persistent freshwater forcing over the North Atlantic, most regions in the North Atlantic show reduced production of  $\text{CaCO}_3$ , opal and POC (Fig. 8). Productivity in the North Atlantic is suggested to be halved during AMOC collapse because of increased stratification, which reduces nutrient supply from deep ocean (Schmittner, 2005). In our model, the productivity in the mid-latitude North Atlantic is indeed greatly reduced after the freshwater forcing is applied. For example, opal production from  $30^\circ\text{N}$ - $50^\circ\text{N}$  in the Atlantic at the end of HOSING is reduced by 50%~90% of its original value in CTRL. However, opal production increases in high latitude North Atlantic (north of  $50^\circ\text{N}$ ). The pattern of opal production changes with high opal production region shifts northward in HOSING (Fig. 8 d, e and f). These particle flux changes will influence sediment  $^{231}\text{Pa}/^{230}\text{Th}$  as discussed below.

North of  $50^\circ\text{N}$  in the Atlantic, opal productivity increases during AMOC\_off (Fig. 8f) and will result an increase in sediment  $^{231}\text{Pa}/^{230}\text{Th}$ . The increase caused by greater opal productivity enhances the sediment  $^{231}\text{Pa}/^{230}\text{Th}$  increase caused by reduced AMOC. Therefore, the increase in p-coupled sediment  $^{231}\text{Pa}/^{230}\text{Th}$  from AMOC\_on to AMOC\_off is larger than p-fixed sediment  $^{231}\text{Pa}/^{230}\text{Th}$  change (Fig.9c).

In the mid-latitude North Atlantic, opal productivity decreases during AMOC\_off (Fig.8 f) and will lead to a decrease in sediment  $^{231}\text{Pa}/^{230}\text{Th}$ , which is opposite to the effect of reduced AMOC. P-coupled sediment  $^{231}\text{Pa}/^{230}\text{Th}$  shows an initial decrease in first 200 years (Fig.9 d, e, and f, red dash lines) caused by the reduced opal productivity. But this decrease trend is reversed eventually, suggesting that the influence of particle flux change is overwhelmed by the effect of reduced AMOC. In the long run, most regions in the subtropical and mid-latitude Atlantic show increased sediment  $^{231}\text{Pa}/^{230}\text{Th}$  in HOSING (Fig.10 d), indicating the dominant effect of reduced AMOC. However, sediment  $^{231}\text{Pa}/^{230}\text{Th}$  at  $40^\circ\text{N}$  west Atlantic, where opal productivity is maximum during AMOC\_on, show a decrease from

AMOC\_on to AMOC\_off (Fig.9 d and Fig.10 d). During AMOC\_on, the opal productivity maximum at 40°N west Atlantic lead to regional maximum sediment  $^{231}\text{Pa}/^{230}\text{Th}$  because of the particle flux effect (Fig. 4). During AMOC\_off, this opal productivity maximum is eliminated (Fig.8 e) and there is no more extra  $^{231}\text{Pa}$  supplied by surroundings to this region, which leads to a decrease in sediment  $^{231}\text{Pa}/^{230}\text{Th}$ . This decrease in sediment  $^{231}\text{Pa}/^{230}\text{Th}$  caused by productivity change is greater than the increase caused by the reduced AMOC. Therefore, sediment  $^{231}\text{Pa}/^{230}\text{Th}$  experiences a decrease from AMOC\_on to AMOC\_off at this location (Fig.9 d and Fig.10 d). Our results suggest that although the circulation effect is more dominant than the particle flux change in controlling sediment  $^{231}\text{Pa}/^{230}\text{Th}$  on long time scale over most of North Atlantic (Fig. 11), particle flux change can be important on short time scale and in high productivity regions. With p-fixed and p-coupled  $^{231}\text{Pa}$  and  $^{230}\text{Th}$ , our model can help to detangle the circulation effect and particle flux effect.

It has been suggested that the particulate  $^{231}\text{Pa}/^{230}\text{Th}$  response to the change of AMOC depends on the location and depth. Above 2km and high latitude North Atlantic, particulate  $^{231}\text{Pa}/^{230}\text{Th}$  decreases with the increased AMOC (Rempfer et al., 2017). Our results are consistent with this finding (Fig. 12 a and b). Both p-fixed and p-coupled particulate  $^{231}\text{Pa}/^{230}\text{Th}$  show similar patterns of change from AMOC\_on to AMOC\_off: decrease in particulate  $^{231}\text{Pa}/^{230}\text{Th}$  at shallow depth and north of 60°N and increase in particulate  $^{231}\text{Pa}/^{230}\text{Th}$  below 2km and south of 60°N during AMOC\_off. Therefore, sediment depth should also be taken into consideration when interpreting sediment  $^{231}\text{Pa}/^{230}\text{Th}$ . Since the pattern in p-coupled is similar to the pattern in p-fixed, the opposite particulate  $^{231}\text{Pa}/^{230}\text{Th}$  changes in shallow and deep North Atlantic is associated with AMOC change. During AMOC\_on, upper limb of AMOC (about upper 1km) transport water northward, which provides extra  $^{231}\text{Pa}$  to North Atlantic and particulate  $^{231}\text{Pa}/^{230}\text{Th}$  is larger than the production ratio of 0.093. In contrast, the lower limb of AMOC (2km-3km) features southward transport, which transports  $^{231}\text{Pa}$  to the Southern Ocean and particulate  $^{231}\text{Pa}/^{230}\text{Th}$  is smaller than the production ratio of 0.093 (Fig. 12 solid). Particulate  $^{231}\text{Pa}/^{230}\text{Th}$  decreases with depth (Fig. 12 c solid). During AMOC\_off, ocean transport of  $^{231}\text{Pa}$  is

greatly reduced. Therefore, shallow (deep) depth experiences a decrease (increase) in particulate  $^{231}\text{Pa}/^{230}\text{Th}$  and the vertical gradient in the particulate  $^{231}\text{Pa}/^{230}\text{Th}$  is also greatly reduced (Fig. 12 c dash). Our results support that the depth dependence of particulate  $^{231}\text{Pa}/^{230}\text{Th}$  is mainly caused by lateral transport of  $^{231}\text{Pa}$  by circulation (Gherardi et al., 2009; Lippold et al., 2011, 2012a; Luo et al., 2010; Rempfer et al., 2017).

Overall, our model is able to simulate the correct magnitude of the sediment  $^{231}\text{Pa}/^{230}\text{Th}$  ratio response to the freshwater forcing. Our experiments suggest that the change of circulation is the dominant factor that influences sediment  $^{231}\text{Pa}/^{230}\text{Th}$  on long time scale over most of the globe in the idealized hosing experiment, although the detailed difference between p-fixed and p-coupled sediment  $^{231}\text{Pa}/^{230}\text{Th}$  ratio response to freshwater forcing in different locations can be complicated.

## 5. Summary

$^{231}\text{Pa}$  and  $^{230}\text{Th}$  have been implemented in the ocean model of the CESM in both the p-coupled and p-fixed forms. Our control experiment under present day climate forcing is able to simulate most  $^{231}\text{Pa}$  and  $^{230}\text{Th}$  water column activity and sediment  $^{231}\text{Pa}/^{230}\text{Th}$  activity ratio consistent with observations by using the parameters that are suggested by Chase et al., (2002) and used in Siddall et al. (2005). Our sensitivity experiments with varying parameters suggest that these parameters are of the right order of magnitude.

Furthermore, our model is able to simulate the overall sediment  $^{231}\text{Pa}/^{230}\text{Th}$  ratio change in the North Atlantic with a magnitude comparable to the reconstruction in response to the collapse of AMOC, although the detailed response can be complicated in different regions. Finally, the p-fixed form is able to capture many major features of that of the p-coupled form over large ocean areas on long time scale, although the two forms can also differ significantly in some regions, especially the region with high opal productivity.

Much remains to be improved in our  $^{231}\text{Pa}$  and  $^{230}\text{Th}$  module in the future. For example, the model can be further improved by including nepheloid layers to better simulate water column  $^{231}\text{Pa}$  and  $^{230}\text{Th}$  activity as in Rempfer et al. (2017). In addition, partition coefficient for different particles can be further tuned, which can improve our understanding of the affinity of  $^{231}\text{Pa}$  and  $^{230}\text{Th}$  to different particles, complementing the limited observational studies available (e.g. Chase et al., 2002; Scholten et al., 2005; Walter et al., 1997). At present, as the first attempt to implement  $^{231}\text{Pa}$  and  $^{230}\text{Th}$  in the CESM with both p-fixed and p-coupled versions, our model can serve as a useful tool to improve our understanding of the processes of  $^{231}\text{Pa}$  and  $^{230}\text{Th}$  as well as interpretations of sediment  $^{231}\text{Pa}/^{230}\text{Th}$  reconstructions for past ocean circulation and climate changes.

#### **Code availability:**

The  $^{231}\text{Pa}$  and  $^{230}\text{Th}$  isotope source code of both p-fixed and p-coupled versions for CESM1.3 is included as supplementary material here.

#### **Acknowledgement:**

This work is supported by NSF P2C2 program (NSF 1401778 and NSF1600080), DOE DE-SC0006744 and NSFC 41630527 and 41130105. Computing resources (ark:/85065/d7wd3xhc) were provided by the Climate Simulation Laboratory at NCAR's Computational and Information Systems Laboratory, sponsored by the National Science Foundation and other agencies.

#### **References:**

- Anderson, R. F., Bacon, M. P. and Brewer, P. G.: Removal of  $^{230}\text{Th}$  and  $^{231}\text{Pa}$  from the open ocean, *Earth Planet. Sci. Lett.*, 62(1), 7–23, doi:10.1016/0012-821X(83)90067-5, 1983.
- Anderson, R. F., Lao, Y., Broecker, W. S., Trumbore, S. E., Hofmann, H. J. and Wolfli, W.: Boundary scavenging in the Pacific Ocean: A comparison of  $^{10}\text{Be}$  and  $^{231}\text{Pa}$ , *Earth Planet. Sci. Lett.*, 96(3–4), 287–304, doi:10.1016/j.cognition.2008.05.007, 1990.
- Anderson, R. F., Fleisher, M. Q., Biscaye, P. E., Kumar, N., Dittrich, B., Kubik, P. and Suter, M.: Anomalous boundary scavenging in the Middle Atlantic Bight: evidence

544 from  $^{230}\text{Th}$ ,  $^{231}\text{Pa}$ ,  $^{10}\text{Be}$  and  $^{210}\text{Pb}$ , *Deep. Res. Part II*, 41(2–3), 537–561,  
 545 doi:10.1016/0967-0645(94)90034-5, 1994.  
 546 Armstrong, R. A., Lee, C., Hedges, J. I., Honjo, S. and Wakeham, S. G.: A new,  
 547 mechanistic model for organic carbon fluxes in the ocean based on the quantitative  
 548 association of POC with ballast minerals, *Deep. Res. Part II Top. Stud. Oceanogr.*,  
 549 49(1–3), 219–236, doi:10.1016/S0967-0645(01)00101-1, 2002.  
 550 Arsouze, T., Dutay, J.-C., Lacan, F. and Jeandel, C.: Reconstructing the Nd oceanic  
 551 cycle using a coupled dynamical – biogeochemical model, *Biogeosciences*, 6(12),  
 552 2829–2846, doi:10.5194/bg-6-2829-2009, 2009.  
 553 Bacon, M. and Anderson, R.: Distribution of Thorium Isotopes between dissolved  
 554 and particulate forms in the deep sea, *J. Geophys. Res. ...*, 87(1), 2045–2056, 1982.  
 555 Bacon, M. P. and Rosholt, J. N.: Accumulation rates of  $^{230}\text{Th}$ ,  $^{231}\text{Pa}$ , and some  
 556 transition metals on the Bermuda Rise, *Geochim. Cosmochim. Acta*, 46, 651–666,  
 557 1982.  
 558 Bacon, M. P., Huh, C. A. and Moore, R. M.: Vertical profiles of some natural  
 559 radionuclides over the Alpha Ridge, Arctic Ocean, *Earth Planet. Sci. Lett.*, 95(1–2),  
 560 15–22, doi:10.1016/0012-821X(89)90164-7, 1989.  
 561 Bradtmiller, L. I., Anderson, R. F., Fleisher, M. Q. and Burckle, L. H.: Opal burial in the  
 562 equatorial Atlantic Ocean over the last 30 ka: Implications for glacial-interglacial  
 563 changes in the ocean silicon cycle, *Paleoceanography*, 22(4), 1–15,  
 564 doi:10.1029/2007PA001443, 2007.  
 565 Bradtmiller, L. I., McManus, J. F. and Robinson, L. F.:  $^{231}\text{Pa}/^{230}\text{Th}$  evidence for a  
 566 weakened but persistent Atlantic meridional overturning circulation during  
 567 Heinrich Stadial 1, *Nat. Commun.*, 5, 5817, doi:10.1038/ncomms6817, 2014.  
 568 Burckel, P., Waelbroeck, C., Luo, Y., Roche, D. M., Pichat, S., Jaccard, S. L., Gherardi, J.,  
 569 Govin, A., Lippold, J. and Thil, F.: Changes in the geometry and strength of the  
 570 Atlantic meridional overturning circulation during the last glacial (20–50 ka), *Clim.*  
 571 *Past*, 12(11), 2061–2075, doi:10.5194/cp-12-2061-2016, 2016.  
 572 Chase, Z. and Robert F, A.: Comment on “On the importance of opal, carbonate, and  
 573 lithogenic clays in scavenging and fractionating  $^{230}\text{Th}$ ,  $^{231}\text{Pa}$  and  $^{10}\text{Be}$  in the ocean”  
 574 by S. Luo and T.-L. Ku, *Earth Planet. Sci. Lett.*, 220(1–2), 201–211,  
 575 doi:10.1016/S0012-821X(04)00027-5, 2004.  
 576 Chase, Z., Anderson, R. F., Fleisher, M. Q. and Kubik, P. W.: The influence of particle  
 577 composition and particle flux on scavenging of Th, Pa and Be in the ocean, *Earth*  
 578 *Planet. Sci. Lett.*, 204(1–2), 215–229, doi:10.1016/S0012-821X(02)00984-6, 2002.  
 579 Cochran, J. K., Livingston, H. D., Hirschberg, D. J. and Surprenant, L. D.: Natural and  
 580 anthropogenic radionuclide distributions in the northwest Atlantic Ocean, *Earth*  
 581 *Planet. Sci. Lett.*, 84(2–3), 135–152, doi:10.1016/0012-821X(87)90081-1, 1987.  
 582 Cochran, J. K., Hirschberg, D. J., Livingston, H. D., Buesseler, K. O. and Key, R. M.:  
 583 Natural and anthropogenic radionuclide distributions in the Nansen Basin, Arctic  
 584 Ocean: Scavenging rates and circulation timescales, *Deep. Res. Part II*, 42(6), 1495–  
 585 1517, doi:10.1016/0967-0645(95)00051-8, 1995.  
 586 Colley, S., Thomson, J. and Newton, P. P.: Detailed Th-230, Th-232 and Pb-210 fluxes  
 587 recorded by the 1989/90 BOFS sediment trap time-series at 48N, 20W, *Deep - Sea*  
 588 *Res. Part I - Oceanogr. Res. Pap.*, 42(6), 833–848, 1995.  
 589 Coppola, L., Roy-Barman, M., Mulsow, S., Povinec, P. and Jeandel, C.: Thorium

isotopes as tracers of particles dynamics and deep water circulation in the Indian sector of the Southern Ocean (ANTARES IV), *Mar. Chem.*, 100(3–4 SPEC. ISS.), 299–313, doi:10.1016/j.marchem.2005.10.019, 2006.

Danabasoglu, G., Bates, S. C., Briegleb, B. P., Jayne, S. R., Jochum, M., Large, W. G., Peacock, S. and Yeager, S. G.: The CCSM4 ocean component, *J. Clim.*, 25(5), 1361–1389, doi:10.1175/JCLI-D-11-00091.1, 2012.

DeMaster, D. J.: The marine budgets of silica and  $^{32}\text{Si}$ , Yale., 1979.

Deng, F., Thomas, A. L., Rijkenberg, M. J. A. and Henderson, G. M.: Controls on seawater  $^{231}\text{Pa}$ ,  $^{230}\text{Th}$  and  $^{232}\text{Th}$  concentrations along the flow paths of deep waters in the Southwest Atlantic, *Earth Planet. Sci. Lett.*, 390, 93–102, doi:10.1016/j.epsl.2013.12.038, 2014.

Doney, S. C., Lima, I., Feely, R. A., Glover, D. M., Lindsay, K., Mahowald, N., Moore, J. K. and Wanninkhof, R.: Mechanisms governing interannual variability in upper-ocean inorganic carbon system and air-sea  $\text{CO}_2$  fluxes: Physical climate and atmospheric dust, *Deep. Res. Part II Top. Stud. Oceanogr.*, 56(8–10), 640–655, doi:10.1016/j.dsr2.2008.12.006, 2009.

Dutay, J.-C., Lacan, F., Roy-Barman, M. and Bopp, L.: Influence of particle size and type on  $^{231}\text{Pa}$  and  $^{230}\text{Th}$  simulation with a global coupled biogeochemical-ocean general circulation model: A first approach, *Geochemistry, Geophys. Geosystems*, 10(1), doi:10.1029/2008GC002291, 2009.

Edmonds, H. N., Moran, S. B., Hoff, J. A., Smith, J. N. and Edwards, R. L.: Protactinium-231 and Thorium-230 Abundances and High Scavenging Rates in the Western Arctic Ocean, *Science* (80-. ), 280(5362), 405–407, doi:10.1126/science.280.5362.405, 1998.

Edmonds, H. N., Moran, S. B., Cheng, H. and Edwards, R. L.:  $^{230}\text{Th}$  and  $^{231}\text{Pa}$  in the Arctic Ocean: Implications for particle fluxes and basin-scale Th/Pa fractionation, *Earth Planet. Sci. Lett.*, 227(1–2), 155–167, doi:10.1016/j.epsl.2004.08.008, 2004.

Francois, R., Bacon, M. P., Altabet, M. A. and Labeyrie, L. D.: Glacial/interglacial changes in sediment rain rate in the SW Indian Sector of subantarctic Waters as recorded by  $^{230}\text{Th}$ ,  $^{231}\text{Pa}$ , U, and  $\delta^{15}\text{N}$ , *Paleoceanography*, 8(5), 611–629, doi:10.1029/93PA00784, 1993.

Frank, M.: Reconstruction of Late Quaternary environmental conditions applying the natural radionuclides  $^{230}\text{Th}$ ,  $^{10}\text{Be}$ ,  $^{231}\text{Pa}$  and  $^{238}\text{U}$ : A study of deep-sea sediments from the eastern sector of the Antarctic Circumpolar Current System, Alfred Wegener Institute for Polar and Marine Research., 1996.

Frank, M., Eisenhauer, A., Kubik, P. W., Ditttrich-hannen, B. and Segl, M.: Beryllium 10, thorium 230, and protactinium 231 in Galapagos microplate sediments: Implications of hydrothermal activity and paleoproductivity changes during the last 100,000 years, *Palaeogeography*, 9(4), 559–578, 1994.

Geibert, W. and Usbeck, R.: Adsorption of thorium and protactinium onto different particle types: Experimental findings, *Geochim. Cosmochim. Acta*, 68(7), 1489–1501, doi:10.1016/j.gca.2003.10.011, 2004.

Gherardi, J., Labeyrie, L., Mcmanus, J., Francois, R., Skinner, L. and Cortijo, E.: Evidence from the Northeastern Atlantic basin for variability in the rate of the meridional overturning circulation through the last deglaciation, *Earth Planet. Sci. Lett.*, 240(3–4), 710–723, doi:10.1016/j.epsl.2005.09.061, 2005.



636 Gherardi, J.-M., Labeyrie, L., Nave, S., Francois, R., McManus, J. F. and Cortijo, E.:  
 637 Glacial-interglacial circulation changes inferred from  $^{231}\text{Pa}/^{230}\text{Th}$  sedimentary  
 638 record in the North Atlantic region, *Paleoceanography*, 24(2),  
 639 doi:10.1029/2008PA001696, 2009.  
 640 Gu, S., Liu, Z., Zhang, J., Rempfer, J., Joos, J., Brady, E. and Oppo, D.: Coherent response  
 641 of Antarctic Intermediate Water and Atlantic Meridional Overturning Circulation  
 642 during the last deglaciation, *Palaeogeography*, doi:10.1002/2017PA003092, 2017.  
 643 Guo, L., Santschi, P. H., Baskaran, M. and Zindler, A.: Distribution of dissolved and  
 644 particulate  $^{230}\text{Th}$  and  $^{232}\text{Th}$  in seawater from the Gulf of Mexico and off Cape  
 645 Hatteras as measured by SIMS, *Earth Planet. Sci. Lett.*, 133(1), 117–128, 1995.  
 646 Gutjahr, M., Frank, M., Stirling, C. H., Keigwin, L. D. and Halliday, a. N.: Tracing the Nd  
 647 isotope evolution of North Atlantic Deep and Intermediate Waters in the western  
 648 North Atlantic since the Last Glacial Maximum from Blake Ridge sediments, *Earth*  
 649 *Planet. Sci. Lett.*, 266(1–2), 61–77, doi:10.1016/j.epsl.2007.10.037, 2008.  
 650 Hall, I. R., Moran, S. B., Zahn, R., Knutz, P. C., Shen, C.-C. and Edwards, R. L.:  
 651 Accelerated drawdown of meridional overturning in the late-glacial Atlantic  
 652 triggered by transient pre-H event freshwater perturbation, *Geophys. Res. Lett.*,  
 653 33(16), L16616, doi:10.1029/2006GL026239, 2006.  
 654 Hayes, C. T., Anderson, R. F., Fleisher, M. Q., Serno, S., Winckler, G. and Gersonde, R.:  
 655 Quantifying lithogenic inputs to the North Pacific Ocean using the long-lived  
 656 thorium isotopes, *Earth Planet. Sci. Lett.*, 383, 16–25,  
 657 doi:10.1016/j.epsl.2013.09.025, 2013.  
 658 Hayes, C. T., Anderson, R. F., Fleisher, M. Q., Huang, K. F., Robinson, L. F., Lu, Y., Cheng,  
 659 H., Edwards, R. L. and Moran, S. B.:  $^{230}\text{Th}$  and  $^{231}\text{Pa}$  on GEOTRACES GA03, the U.S.  
 660 GEOTRACES North Atlantic transect, and implications for modern and  
 661 paleoceanographic chemical fluxes, *Deep. Res. Part II Top. Stud. Oceanogr.*, 116, 29–  
 662 41, doi:10.1016/j.dsr2.2014.07.007, 2015.  
 663 Henderson, G. M. and Anderson, R. F.: The U-series toolbox for paleoceanography,  
 664 *Rev. Mineral. Geochemistry*, 52(1), 493–531, doi:10.2113/0520493, 2003.  
 665 Henderson, G. M., Heinze, C., Anderson, R. F. and Winguth, A. M. E.: Global  
 666 distribution of the  $^{230}\text{Th}$  flux to ocean sediments constrained by GCM modelling,  
 667 *Deep. Res. Part I Oceanogr. Res. Pap.*, 46(11), 1861–1893, doi:10.1016/S0967-  
 668 0637(99)00030-8, 1999.  
 669 Hoffmann, S. S., McManus, J. F., Curry, W. B. and Brown-Leger, L. S.: Persistent export  
 670 of  $^{231}\text{Pa}$  from the deep central Arctic Ocean over the past 35,000 years., *Nature*,  
 671 497(7451), 603–6, doi:10.1038/nature12145, 2013.  
 672 Hsieh, Y. Te, Henderson, G. M. and Thomas, A. L.: Combining seawater  $^{232}\text{Th}$  and  
 673  $^{230}\text{Th}$  concentrations to determine dust fluxes to the surface ocean, *Earth Planet.*  
 674 *Sci. Lett.*, 312(3–4), 280–290, doi:10.1016/j.epsl.2011.10.022, 2011.  
 675 Huh, C. A. and Beasley, T. M.: Profiles of dissolved and particulate thorium isotopes  
 676 in the water column of coastal Southern California, *Earth Planet. Sci. Lett.*, 85(1–3),  
 677 1–10, doi:10.1016/0012-821X(87)90016-1, 1987.  
 678 Hurrell, J. W., Holland, M. M., Gent, P. R., Ghan, S., Kay, J. E., Kushner, P. J., Lamarque, J.  
 679 F., Large, W. G., Lawrence, D., Lindsay, K., Lipscomb, W. H., Long, M. C., Mahowald, N.,  
 680 Marsh, D. R., Neale, R. B., Rasch, P., Vavrus, S., Vertenstein, M., Bader, D., Collins, W. D.,  
 681 Hack, J. J., Kiehl, J. and Marshall, S.: The community earth system model: A

682 framework for collaborative research, *Bull. Am. Meteorol. Soc.*, 94(9), 1339–1360,  
 683 doi:10.1175/BAMS-D-12-00121.1, 2013.  
 684 Jahn, A., Lindsay, K., Giraud, X., Gruber, N., Otto-Bliesner, B. L., Liu, Z. and Brady, E. C.:  
 685 Carbon isotopes in the ocean model of the Community Earth System Model (CESM1),  
 686 *Geosci. Model Dev.*, 8(8), 2419–2434, doi:10.5194/gmd-8-2419-2015, 2015.  
 687 Jonkers, L., Zahn, R., Thomas, A., Henderson, G., Abouchami, W., Francois, R.,  
 688 Masque, P., Hall, I. R. and Bickert, T.: Deep circulation changes in the central South  
 689 Atlantic during the past 145 kyrs reflected in a combined  $^{231}\text{Pa}/^{230}\text{Th}$ ,  
 690 Neodymium isotope and benthic  $\delta^{13}\text{C}$  record, *Earth Planet. Sci. Lett.*, 419, 14–21,  
 691 doi:10.1016/j.epsl.2015.03.004, 2015.  
 692 Keigwin, L. D. and Boyle, E. A.: Did North Atlantic overturning halt 17,000 years ago?,  
 693 *Paleoceanography*, 23(1), 1–5, doi:10.1029/2007PA001500, 2008.  
 694 Kriest, I.: Different parameterizations of marine snow in a 1D-model and their  
 695 influence on representation of marine snow, nitrogen budget and sedimentation,  
 696 *Deep. Res. Part I Oceanogr. Res. Pap.*, 49(12), 2133–2162, doi:10.1016/S0967-  
 697 0637(02)00127-9, 2002.  
 698 Ku, T. L.: Uranium series disequilibrium in deep sea sediments, Columbia., 1966.  
 699 Ku, T. L., Bischoff, J. L. and Boersma, A.: Age studies of Mid-Atlantic Ridge sediments  
 700 near  $42^{\circ}\text{N}$  and  $20^{\circ}\text{N}$ , *Deep. Res. Oceanogr. Abstr.*, 19(3), 233–247,  
 701 doi:10.1016/0011-7471(72)90033-2, 1972.  
 702 Kumar, N.: Trace metals and natural radionuclides as tracers of ocean productivity,  
 703 Columbia., 1994.  
 704 Kumar, N., Gwiazda, R., Anderson, R. F. and Froelich, P. N.:  $^{231}\text{Pa}/^{230}\text{Th}$  ratios in  
 705 sediments as a proxy for past changes in Southern Ocean productivity, *Nature*, 362,  
 706 45–48, doi:10.1038/362045a0, 1993.  
 707 Large, W. G. and Yeager, S. G.: The global climatology of an interannually varying air-  
 708 sea flux data set, *Clim. Dyn.*, 33(2–3), 341–364, doi:10.1007/s00382-008-0441-3,  
 709 2008.  
 710 Lippold, J., Grützner, J., Winter, D., Lahaye, Y., Mangini, A. and Christi, M.: Does  
 711 sedimentary  $^{231}\text{Pa}/^{230}\text{Th}$  from the Bermuda Rise monitor past Atlantic Meridional  
 712 Overturning Circulation?, *Geophys. Res. Lett.*, 36(12), 1–6,  
 713 doi:10.1029/2009GL038068, 2009.  
 714 Lippold, J., Gherardi, J. M. and Luo, Y.: Testing the  $^{231}\text{Pa}/^{230}\text{Th}$  paleocirculation proxy:  
 715 A data versus 2D model comparison, *Geophys. Res. Lett.*, 38(20), 1–7,  
 716 doi:10.1029/2011GL049282, 2011.  
 717 Lippold, J., Mulitza, S., Mollenhauer, G., Weyer, S., Heslop, D. and Christl, M.:  
 718 Boundary scavenging at the East Atlantic margin does not negate use of  $^{231}\text{Pa}/$   
 719  $^{230}\text{Th}$  to trace Atlantic overturning, *Earth Planet. Sci. Lett.*, 333–334, 317–331,  
 720 doi:10.1016/j.epsl.2012.04.005, 2012a.  
 721 Lippold, J., Luo, Y., Francois, R., Allen, S. E., Gherardi, J., Pichat, S., Hickey, B. and  
 722 Schulz, H.: Strength and geometry of the glacial Atlantic Meridional Overturning  
 723 Circulation, *Nat. Geosci.*, 5(11), 813–816, doi:10.1038/ngeo1608, 2012b.  
 724 Long, M. C., Lindsay, K., Peacock, S., Moore, J. K. and Doney, S. C.: Twentieth-century  
 725 oceanic carbon uptake and storage in CESM1(BGC), *J. Clim.*, 26(18), 6775–6800,  
 726 doi:10.1175/JCLI-D-12-00184.s1, 2013.  
 727 Luo, S. and Ku, T. L.: Oceanic  $^{231}\text{Pa}/^{230}\text{Th}$  ratio influenced by particle composition

728 and remineralization, *Earth Planet. Sci. Lett.*, 167(3–4), 183–195,  
 729 doi:10.1016/S0012-821X(99)00035-7, 1999.  
 730 Luo, S. D., Ku, T. L., Kusakabe, M., Bishop, J. K. B. and Yang, Y. L.: Tracing particle  
 731 cycling in the upper ocean with Th-230 and Th-228: An investigation in the  
 732 equatorial Pacific along 140 degrees W, *Deep - Sea Res. Part II - Top. Stud. Oceanogr.*,  
 733 42(2–3), 805–829, doi:10.1016/0967-0645(95)00019-M, 1995.  
 734 Luo, Y., Francois, R. and Allen, S.: Sediment <sup>231</sup>Pa/<sup>230</sup>Th as a recorder of the rate of  
 735 the Atlantic meridional overturning circulation: insights from a 2-D model, *Ocean*  
 736 *Sci.*, 6(3), 381–400, doi:10.5194/os-6-381-2010, 2010.  
 737 Mangini, A. and Diester-Hass, L.: Excess Th-230 in sediments off NW Africa traces  
 738 upwelling during the past 130,000 years, in *Coastal upwelling: Its sedimentary*  
 739 *records*, edited by E. Suess and J. Thiede, pp. 455–470, Plenum., 1983.  
 740 Mangini, A. and Key, R. M.: A <sup>230</sup>Th profile in the Atlantic Ocean, *Earth Planet. Sci.*  
 741 *Lett.*, 62(3), 377–384, doi:10.1016/0012-821X(83)90008-0, 1983.  
 742 Mangini, A. and Sonntag, C.: <sup>231</sup>Pa dating of deep-sea cores via <sup>227</sup>Th counting,  
 743 *Earth Planet. Sci. Lett.*, 37(2), 251–256, 1977.  
 744 Mangini, A. and U., K.: Depositional history in the Clarion-Clipperton zone during the  
 745 last 250,000 years: <sup>230</sup>Th and <sup>231</sup>Pa methods, *Geol. Jahrb.*, 87, 105–121, 1987.  
 746 Marchal, O., François, R., Stocker, T. F. and Joos, F.: Ocean thermohaline circulation  
 747 and sedimentary <sup>231</sup>Pa/<sup>230</sup>Th ratio, *Paleoceanography*, 15(6), 625–641 [online]  
 748 Available from: <http://onlinelibrary.wiley.com/doi/10.1029/2000PA000496/full>  
 749 (Accessed 19 April 2016), 2000.  
 750 McManus, J., Francois, R. and Gherardi, J.: Collapse and rapid resumption of Atlantic  
 751 meridional circulation linked to deglacial climate changes, *Nature*, 428(6985), 834–  
 752 837, 2004.  
 753 Moore, J. K. and Braucher, O.: Sedimentary and mineral dust sources of dissolved  
 754 iron to the World Ocean, *Biogeosciences*, 5(1994), 631–656, doi:10.5194/bgd-4-  
 755 1279-2007, 2008.  
 756 Moore, J. K., Doney, S. C., Glover, D. M. and Fung, I. Y.: Iron cycling and nutrient-  
 757 limitation patterns in surface waters of the World Ocean, , 49, 463–507, 2002.  
 758 Moore, J. K., Doney, S. C. and Lindsay, K.: Upper ocean ecosystem dynamics and iron  
 759 cycling in a global three-dimensional model, *Global Biogeochem. Cycles*, 18(4),  
 760 doi:10.1029/2004GB002220, 2004.  
 761 Moore, J. K., Lindsay, K., Doney, S. C., Long, M. C. and Misumi, K.: Marine Ecosystem  
 762 Dynamics and Biogeochemical Cycling in the Community Earth System Model  
 763 [CESM1(BGC)]: Comparison of the 1990s with the 2090s under the RCP4.5 and  
 764 RCP8.5 Scenarios, *J. Clim.*, 26(23), 9291–9312, doi:10.1175/JCLI-D-12-00566.1,  
 765 2013.  
 766 Moore, R. M. and Hunter, K. A.: Thorium adsorption in the ocean: reversibility and  
 767 distribution amongst particle sizes, *Geochim. Cosmochim. Acta*, 49(11), 2253–2257,  
 768 doi:10.1016/0016-7037(85)90225-X, 1985.  
 769 Moore, W. S.: The thorium isotope content of ocean water, *Earth Planet. Sci. Lett.*,  
 770 53(3), 419–426, doi:10.1016/0012-821X(81)90046-7, 1981.  
 771 Moran, S. B., Hoff, J. A., Buesseler, K. O. and Edwards, R. L.: High precision <sup>230</sup>Th and  
 772 <sup>232</sup>Th in the Norwegian Sea and Denmark by thermal ionization mass  
 773 spectrometry, , 22(19), 2589–2592, 1995.

774 Moran, S. B., Charette, M. a., Hoff, J. a., Edwards, R. L. and Landing, W. M.: Distribution  
 775 of  $^{230}\text{Th}$  in the Labrador Sea and its relation to ventilation, *Earth Planet. Sci. Lett.*,  
 776 150, 151–160, doi:10.1016/S0012-821X(97)00081-2, 1997.  
 777 Moran, S. B., Shen, C.-C., Weinstein, S. E., Hettlinger, L. H., Hoff, J. H., Edmonds, H. N.  
 778 and Edwards, R. L.: Constraints on deep water age and particle flux in the Equatorial  
 779 and South Atlantic Ocean based on seawater  $^{231}\text{Pa}$  and  $^{230}\text{Th}$  data, *Geophys. Res.*  
 780 *Lett.*, 28(18), 3437–3440 [online] Available from:  
 781 papers2://publication/uuid/2A811583-B32B-4BD8-B582-EC8B0D96A949, 2001.  
 782 Moran, S. B., Shen, C. C., Edmonds, H. N., Weinstein, S. E., Smith, J. N. and Edwards, R.  
 783 L.: Dissolved and particulate  $^{231}\text{Pa}$  and  $^{230}\text{Th}$  in the Atlantic Ocean: Constraints on  
 784 intermediate/deep water age, boundary scavenging, and  $^{231}\text{Pa}/^{230}\text{Th}$   
 785 fractionation, *Earth Planet. Sci. Lett.*, 203(3–4), 999–1014, doi:10.1016/S0012-  
 786 821X(02)00928-7, 2002.  
 787 Müller, P. J. and Mangini, A.: Organic carbon decomposition rates in sediments of the  
 788 pacific manganese nodule belt dated by  $^{230}\text{Th}$  and  $^{231}\text{Pa}$ , *Earth Planet. Sci. Lett.*,  
 789 51(1), 94–114, doi:10.1016/0012-821X(80)90259-9, 1980.  
 790 Negre, C., Zahn, R., Thomas, A. L., Masqué, P., Henderson, G. M., Martínez-Méndez, G.,  
 791 Hall, I. R. and Mas, J. L.: Reversed flow of Atlantic deep water during the Last Glacial  
 792 Maximum., *Nature*, 468(7320), 84–88, doi:10.1038/nature09508, 2010.  
 793 Nozaki, Y. and Horibe, Y.: Alpha-emitting thorium isotopes in northwest Pacific deep  
 794 waters, *Earth Planet. Sci. Lett.*, 65(1), 39–50, doi:10.1016/0012-821X(83)90188-7,  
 795 1983.  
 796 Nozaki, Y. and Nakanishi, T.:  $^{231}\text{Pa}$  and  $^{230}\text{Th}$  profiles in the open ocean water  
 797 column, *Deep Sea Res. Part A, Oceanogr. Res. Pap.*, 32(10), 1209–1220,  
 798 doi:10.1016/0198-0149(85)90004-4, 1985.  
 799 Nozaki, Y. and Yamada, M.: Thorium and protactinium isotope distributions in  
 800 waters of the Japan Sea, *Deep Sea Res. Part A, Oceanogr. Res. Pap.*, 34(8), 1417–1430,  
 801 1987.  
 802 Nozaki, Y. and Yang, H. S.: Th and Pa isotopes in the waters of the western margin of  
 803 the pacific near Japan: Evidence for release of  $^{228}\text{Ra}$  and  $^{227}\text{Ac}$  from slope  
 804 sediments, *J. Oceanogr. Soc. Japan*, 43(4), 217–227, doi:10.1007/BF02109817, 1987.  
 805 Nozaki, Y., Horibe, Y. and Tsubota, H.: The water column distribution of thorium  
 806 isotopes in the western North Pacific, *Earth Planet. Sci. Lett.*, 54(54), 203–216, 1981.  
 807 Nozaki, Y., Yang, H.-S. and Yamada, M.: Scavenging of thorium in the ocean, *J.*  
 808 *Geophys. Res.*, 92(C1), 772, doi:10.1029/JC092iC01p00772, 1987.  
 809 Okubo, A., Obata, H., Nozaki, Y., Yamamoto, Y. and Minami, H.:  $^{230}\text{Th}$  in the  
 810 Andaman Sea: Rapid deep-sea renewal, *Geophys. Res. Lett.*, 31(22), 1–5,  
 811 doi:10.1029/2004GL020226, 2004.  
 812 Okubo, A., Obata, H., Luo, S., Gamo, T., Yamamoto, Y., Minami, H. and Yamada, M.:  
 813 Particle flux in the twilight zone of the eastern Indian Ocean: A constraint from  
 814  $^{234}\text{U}$ - $^{230}\text{Th}$  and  $^{228}\text{Ra}$ - $^{228}\text{Th}$  disequilibria, *Deep. Res. Part I Oceanogr. Res. Pap.*,  
 815 54(10), 1758–1772, doi:10.1016/j.dsr.2007.06.009, 2007a.  
 816 Okubo, A., Obata, H., Gamo, T., Minami, H. and Yamada, M.: Scavenging of  $^{230}\text{Th}$  in  
 817 the Sulu Sea, *Deep. Res. Part II Top. Stud. Oceanogr.*, 54(1–2), 50–59,  
 818 doi:10.1016/j.dsr2.2006.02.016, 2007b.  
 819 Okubo, A., Obata, H., Gamo, T. and Yamada, M.:  $^{230}\text{Th}$  and  $^{232}\text{Th}$  distributions in

820 mid-latitudes of the North Pacific Ocean: Effect of bottom scavenging, *Earth Planet.*  
 821 *Sci. Lett.*, 339–340, 139–150, doi:10.1016/j.epsl.2012.05.012, 2012.  
 822 Rempfer, J., Stocker, T. F., Joos, F., Lippold, J. and Jaccard, S. L.: New insights into  
 823 cycling of  $^{231}\text{Pa}$  and  $^{230}\text{Th}$  in the Atlantic Ocean, *Earth Planet. Sci. Lett.*, 468, 27–  
 824 37, doi:10.1016/j.epsl.2017.03.027, 2017.  
 825 Roberts, N. L., McManus, J. F., Piotrowski, A. M. and McCave, I. N.: Advection and  
 826 scavenging controls of  $\text{Pa}/\text{Th}$  in the northern NE Atlantic, *Paleoceanography*, 29(6),  
 827 668–679, doi:10.1002/2014PA002633, 2014.  
 828 Robinson, L. F., Belshaw, N. S. and Henderson, G. M.: U and Th concentrations and  
 829 isotope ratios in modern carbonates and waters from the Bahamas, *Geochim.*  
 830 *Cosmochim. Acta*, 68(8), 1777–1789, doi:10.1016/j.gca.2003.10.005, 2004.  
 831 Roy-Barman, M., Chen, J. H. and Wasserburg, G. J.:  $^{230}\text{Th}$ - $^{232}\text{Th}$  systematics in the  
 832 central Pacific Ocean: The sources and the fates of thorium, *Earth Planet. Sci. Lett.*,  
 833 139(3–4), 351–363, doi:10.1016/0012-821X(96)00017-9, 1996.  
 834 Rutgers van der Loeff, M. M. and Berger, G. W.: Scavenging of  $^{230}\text{Th}$  and  $^{231}\text{Pa}$  near  
 835 the antarctic polar front in the South Atlantic, *Deep. Res. Part I*, 40(2), 339–357,  
 836 doi:10.1016/0967-0637(93)90007-P, 1993.  
 837 Schmittner, A.: Decline of the marine ecosystem caused by a reduction in the  
 838 Atlantic overturning circulation., *Nature*, 434(7033), 628–633,  
 839 doi:10.1038/nature03476, 2005.  
 840 Schmitz, W., Mangini, A., Stoffers, P., Glasby, G. P. and Pluger, W. L.: Sediment  
 841 accumulation rates in the southwestern Pacific Basin and Aitutaki Passage, *Mar.*  
 842 *Geol.*, 73(1), 181–190, 1986.  
 843 Scholten, J. C., Rutgers van der Loeff, M. M. and Michel, A.: Distribution of  $^{230}\text{Th}$  and  
 844  $^{231}\text{Pa}$  in the water column in relation to the ventilation of the deep Arctic basins,  
 845 *Deep. Res. Part II*, 42(6), 1519–1531, doi:10.1016/0967-0645(95)00052-6, 1995.  
 846 Scholten, J. C., Fietzke, J., Mangini, A., Stoffers, P., Rixen, T., Gaye-Haake, B., Blanz, T.,  
 847 Ramaswamy, V., Sirocko, F., Schulz, H. and Ittekkot, V.: Radionuclide fluxes in the  
 848 Arabian Sea: The role of particle composition, *Earth Planet. Sci. Lett.*, 230(3–4), 319–  
 849 337, doi:10.1016/j.epsl.2004.11.003, 2005.  
 850 Scholten, J. C., Fietzke, J., Mangini, A., Garbe-Schönberg, C. D., Eisenhauer, A.,  
 851 Schneider, R. and Stoffers, P.: Advection and scavenging: Effects on  $^{230}\text{Th}$  and  
 852  $^{231}\text{Pa}$  distribution off Southwest Africa, *Earth Planet. Sci. Lett.*, 271(1–4), 159–169,  
 853 doi:10.1016/j.epsl.2008.03.060, 2008.  
 854 Shimmield, G. B. and Price, N. B.: The scavenging of U,  $^{230}\text{Th}$  and  $^{231}\text{Pa}$  during  
 855 pulsed hydrothermal activity at 20°S, East Pacific Rise, *Geochim. Cosmochim. Acta*,  
 856 52(3), 669–677, doi:10.1016/0016-7037(88)90329-8, 1988.  
 857 Shimmield, G. B., Murray, J. W., Thomson, J., Bacon, M. P., Anderson, R. F. and Price, N.  
 858 B.: The distribution and behaviour of  $^{230}\text{Th}$  and  $^{231}\text{Pa}$  at an ocean margin, Baja  
 859 California, Mexico, *Geochim. Cosmochim. Acta*, 50(11), 2499–2507,  
 860 doi:10.1016/0016-7037(86)90032-3, 1986.  
 861 Siddall, M., Henderson, G. M., Edwards, N. R., Frank, M., Müller, S. a., Stocker, T. F. and  
 862 Joos, F.:  $^{231}\text{Pa}/^{230}\text{Th}$  fractionation by ocean transport, biogenic particle flux and  
 863 particle type, *Earth Planet. Sci. Lett.*, 237(1–2), 135–155,  
 864 doi:10.1016/j.epsl.2005.05.031, 2005.  
 865 Siddall, M., Stocker, T. F., Henderson, G. M., Joos, F., Frank, M., Edwards, N. R., Ritz, S.

P. and Müller, S. a.: Modeling the relationship between  $^{231}\text{Pa}$ /  $^{230}\text{Th}$  distribution in North Atlantic sediment and Atlantic meridional overturning circulation, *Paleoceanography*, 22(2), n/a-n/a, doi:10.1029/2006PA001358, 2007.

Thomas, A. L., Henderson, G. M. and Robinson, L. F.: Interpretation of the  $^{231}\text{Pa}/^{230}\text{Th}$  paleocirculation proxy: New water-column measurements from the southwest Indian Ocean, *Earth Planet. Sci. Lett.*, 241(3–4), 493–504, doi:10.1016/j.epsl.2005.11.031, 2006.

Trimble, S. M., Baskaran, M. and Porcelli, D.: Scavenging of thorium isotopes in the Canada Basin of the Arctic Ocean, *Earth Planet. Sci. Lett.*, 222(3–4), 915–932, doi:10.1016/j.epsl.2004.03.027, 2004.

Venchiarutti, C., van der Loeff, M. R. and Stimac, I.: Scavenging of  $^{231}\text{Pa}$  and thorium isotopes based on dissolved and size-fractionated particulate distributions at Drake Passage (ANTXXIV-3), *Deep. Res. Part II Top. Stud. Oceanogr.*, 58(25–26), 2767–2784, doi:10.1016/j.dsr2.2010.10.040, 2011.

Vogler, S., Scholten, J., Rutgers van der Loeff, M. M. and Mangini, A.:  $^{230}\text{Th}$  in the eastern North Atlantic: the importance of water mass ventilation in the balance of  $^{230}\text{Th}$ , *Earth Planet. Sci. Lett.*, 156(1–2), 61–74, doi:10.1016/S0012-821X(98)00011-9, 1998.

Walter, H. J., Rutgers van der Loeff, M. M. and Hoeltzen, H.: Enhanced scavenging of  $^{231}\text{Pa}$  relative to  $^{230}\text{Th}$  in the South Atlantic south of the Polar Front: Implications for the use of the  $^{231}\text{Pa}/^{230}\text{Th}$  ratio as a paleoproductivity proxy, *Earth Planet. Sci. Lett.*, 149(1), 85–100, doi:10.1016/S0012-821X(97)00068-X, 1997.

Yang, H. S., Nozaki, Y., Sakai, H. and Masuda, A.: The distribution of  $^{230}\text{Th}$  and  $^{231}\text{Pa}$  in the deep-sea surface sediments of the Pacific Ocean, *Geochim. Cosmochim. Acta*, 50(1), 81–89, doi:10.1016/0016-7037(86)90050-5, 1986.

Yong-Liang Yang, Elderfield, H., Pedersen, T. F. and Ivanovich, M.: Geochemical record of the Panama Basin during the Last Glacial Maximum carbon event shows that the glacial ocean was not suboxic, *Geology*, 23(12), 1115–1118, doi:10.1130/0091-7613(1995)023<1115:GROTPB>2.3.CO, 1995.

Yong Lao, Anderson, R. F., Broecker, W. S., Trumbore, S. E., Hofmann, H. J. and Wolfli, W.: Transport and burial rates of  $^{10}\text{Be}$  and  $^{231}\text{Pa}$  in the Pacific Ocean during the Holocene period, *Earth Planet. Sci. Lett.*, 113(1–2), 173–189, doi:10.1016/0012-821X(92)90218-K, 1992.

Yu, E.-F.: Variations in the Particulate Flux of  $^{230}\text{Th}$  and  $^{231}\text{Pa}$  and Paleooceanographic Applications of the  $^{231}\text{Pa}/^{230}\text{Th}$  Ratio, WHOI/MIT., 1994.

Yu, E.-F., Francois, R. and Bacon, M. P.: Similar rates of modern and last-glacial ocean thermohaline circulation inferred from radiochemical data, *Nature*, 379(6567), 689–694, doi:10.1038/379689a0, 1996.

Variable	Symbol	Value	Units
Production of $^{231}\text{Pa}$ from U decay	$\beta^{\text{Pa}}$	$2.33 \cdot 10^{-3}$	$\text{dpm m}^{-3} \text{ yr}^{-1}$
Production of $^{230}\text{Th}$ from U decay	$\beta^{\text{Th}}$	$2.52 \cdot 10^{-2}$	$\text{dpm m}^{-3} \text{ yr}^{-1}$
Decay constant of $^{231}\text{Pa}$	$\lambda^{\text{Pa}}$	$2.13 \cdot 10^{-5}$	$\text{yr}^{-1}$
Decay constant of $^{230}\text{Th}$	$\lambda^{\text{Th}}$	$9.22 \cdot 10^{-6}$	$\text{yr}^{-1}$
Index for $^{231}\text{Pa}$ and $^{230}\text{Th}$	i		
Index for particle type	j		
Total isotope activity	$A_t$		$\text{dpm m}^{-3}$
Dissolved isotope activity	$A_d$		$\text{dpm m}^{-3}$
Particle associated activity	$A_p$		$\text{dpm m}^{-3}$
Particle settling velocity	$w_s$	1000	$\text{m yr}^{-1}$
Particle concentration	$C$		$\text{kg m}^{-3}$
Density of seawater		1024.5	$\text{kg m}^{-3}$
Ratio between particle concentration and density of seawater	$R$		

Table 1. List of parameters, abbreviations and values.

	CTRL		EXP_1		EXP_2	
	$^{231}\text{Pa}$	$^{230}\text{Th}$	$^{231}\text{Pa}$	$^{230}\text{Th}$	$^{231}\text{Pa}$	$^{230}\text{Th}$
$K_{\text{CaCO}_3}$	$2.5 \cdot 10^5$	$1.0 \cdot 10^7$	$5 \cdot 10^4$	$2 \cdot 10^6$	$1.25 \cdot 10^6$	$5 \cdot 10^7$
$K_{\text{opal}}$	$1.67 \cdot 10^6$	$5 \cdot 10^5$	$3.33 \cdot 10^5$	$1 \cdot 10^5$	$8.33 \cdot 10^6$	$2.5 \cdot 10^6$
$K_{\text{POC}}$	$1.0 \cdot 10^7$	$1.0 \cdot 10^7$	$2 \cdot 10^6$	$2 \cdot 10^6$	$5 \cdot 10^7$	$5 \cdot 10^7$
$\tau$ (yr)	118	33	501	143	27	9

Table 2. Partition coefficients for different particle types and residence time for  $^{231}\text{Pa}$  and  $^{230}\text{Th}$  in different experiments. Partition coefficients used in CTRL follows (Chase et al., 2002; Siddall et al., 2005). Both p-coupled and p-fixed versions are enabled in CTRL, which yields identical results (discussed in section 4.1). Only p-fixed version is enabled in Exp\_1 and Exp\_2. The residence time ( $\tau$ ) is for p-fixed version in each experiment.

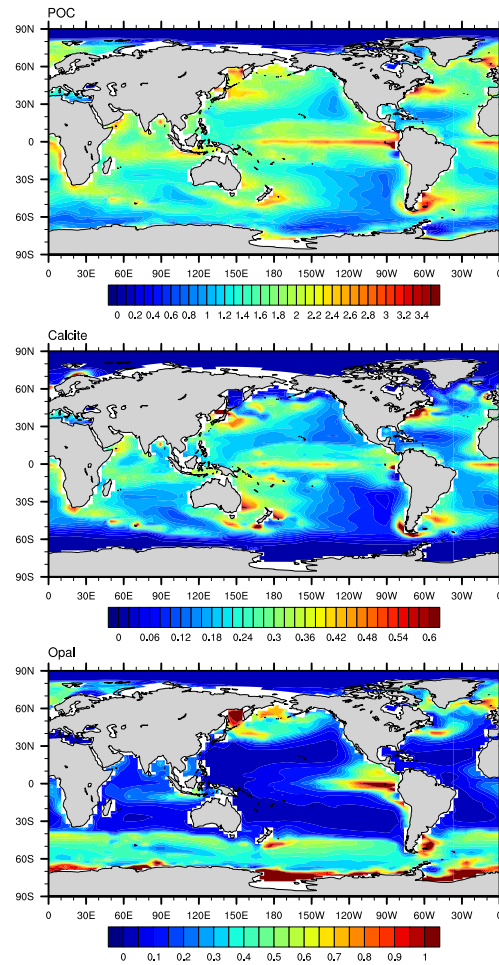
WATER COLUMN ACTIVITY	Holocene core-top $^{231}\text{Pa}/^{230}\text{Th}$
(Guo et al., 1995)	(Yu, 1994)
(Cochran et al., 1987)	(DeMaster, 1979)
(Nozaki et al., 1987)	(Bacon and Rosholt, 1982)
(Bacon and Anderson, 1982)	(Mangini and Diester-Hass, 1983)
(Bacon et al., 1989)	(Kumar, 1994)

(Huh and Beasley, 1987)	(Yang et al., 1986)
(Rutgers van der Loeff and Berger, 1993)	(Anderson et al., 1983)
(Nozaki et al., 1981)	(Anderson et al., 1994)
(Nozaki and Nakanishi, 1985)	(Ku, 1966)
(Mangini and Key, 1983)	(Ku et al., 1972)
(Nozaki and Horibe, 1983)	(Frank et al., 1994)
(Moore, 1981)	(Shimmield et al., 1986)
(Nozaki and Yamada, 1987)	(Frank, 1996)
(Roy-Barman et al., 1996)	(Yong Lao et al., 1992)
(Nozaki and Yang, 1987)	(Francois et al., 1993)
(Moran et al., 1995)	(Anderson et al., 1990)
(Luo et al., 1995)	(Mangini and Sonntag, 1977)
(Colley et al., 1995)	(Schmitz et al., 1986)
(Scholten et al., 1995)	(Shimmield and Price, 1988)
(Cochran et al., 1995)	(Yong-Liang Yang et al., 1995)
(Vogler et al., 1998)	(Müller and Mangini, 1980)
(Moran et al., 1997)	(Mangini and U., 1987)
(Edmonds et al., 1998)	(Scholten et al., 1995)
(Moran et al., 2001)	(Walter et al., 1997)
(Edmonds et al., 2004)	(Lippold et al., 2011)
(Okubo et al., 2007b)	(Lippold et al., 2012b)
(Coppola et al., 2006)	(Bradtmiller et al., 2007)
(Moran et al., 2002)	(Gherardi et al., 2005)
(Okubo et al., 2004)	(Gutjahr et al., 2008)
(Okubo et al., 2007a)	(Hall et al., 2006)
(Okubo et al., 2012)	(Lippold et al., 2011)
(Robinson et al., 2004)	(Roberts et al., 2014)
(Thomas et al., 2006)	(Bradtmiller et al., 2014)
(Trimble et al., 2004)	(Burckel et al., 2016)
(Venchiarutti et al., 2011)	(Hoffmann et al., 2013)
(Hsieh et al., 2011)	(Jonkers et al., 2015)
(Scholten et al., 2008)	(Negre et al., 2010)
(Luo et al., 2010)	
(Deng et al., 2014)	
(Hayes et al., 2013)	
(Hayes et al., 2015)	

Table 3. References for observations of water column  $^{231}\text{Pa}$  and  $^{230}\text{Th}$  activity (left column) and Holocene core-top  $^{231}\text{Pa}/^{230}\text{Th}$  (right column).



922 Figures:

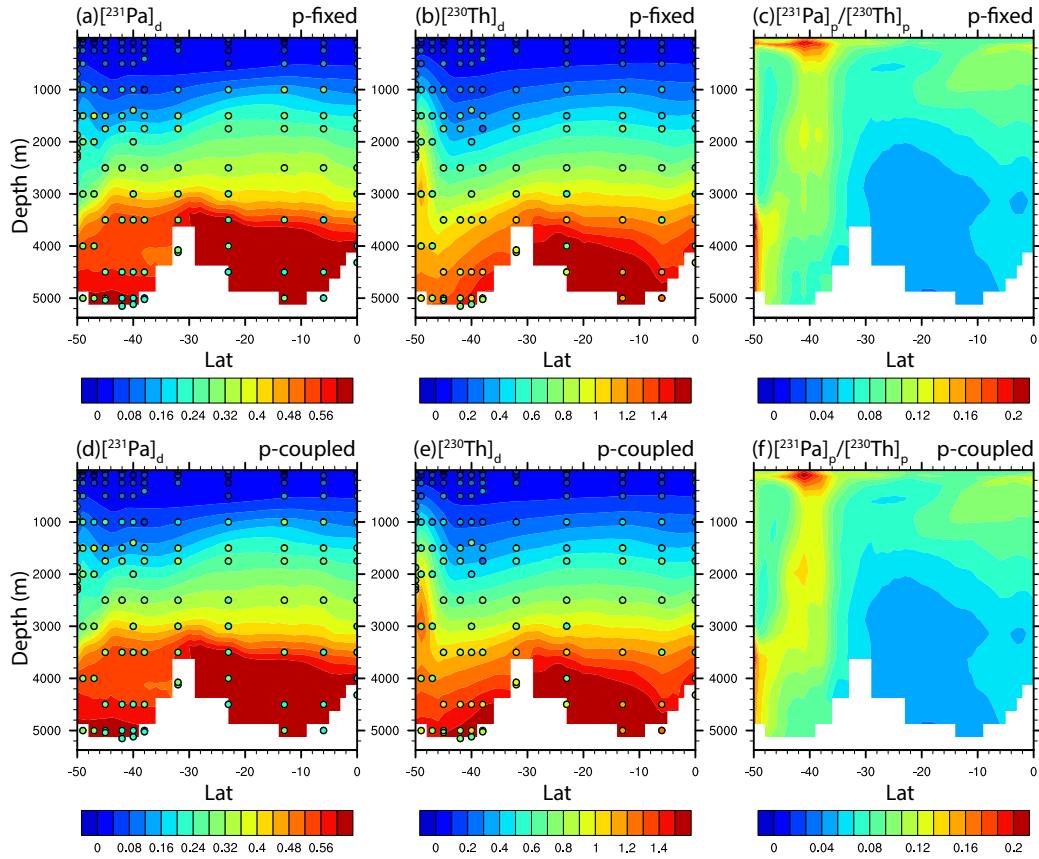


923

924 Figure 1. Annual mean particle fluxes in CESM. (a)  $\text{CaCO}_3$  flux at 105m ( $\text{mol m}^{-2} \text{yr}^{-1}$ ).

925 (b) Opal flux at 105m ( $\text{mol m}^{-2} \text{yr}^{-1}$ ). (c) POC flux at 105m ( $\text{mol m}^{-2} \text{yr}^{-1}$ ).

926



929 Figure 2. Dissolved  $^{231}\text{Pa}$ , dissolved  $^{230}\text{Th}$  and particulate  $^{231}\text{Pa}/^{230}\text{Th}$  in CTRL along  
 930 GEOTRACES transect GA02S (Deng et al., 2014) (the track is indicated in Fig. S4) for  
 931 both p-fixed (top row) and p-coupled (bottom row)  $^{231}\text{Pa}$  and  $^{230}\text{Th}$  (colored  
 932 contour). Observations of dissolved  $^{231}\text{Pa}$  and  $^{230}\text{Th}$  activity are superimposed as  
 933 colored circles using the same color scale.

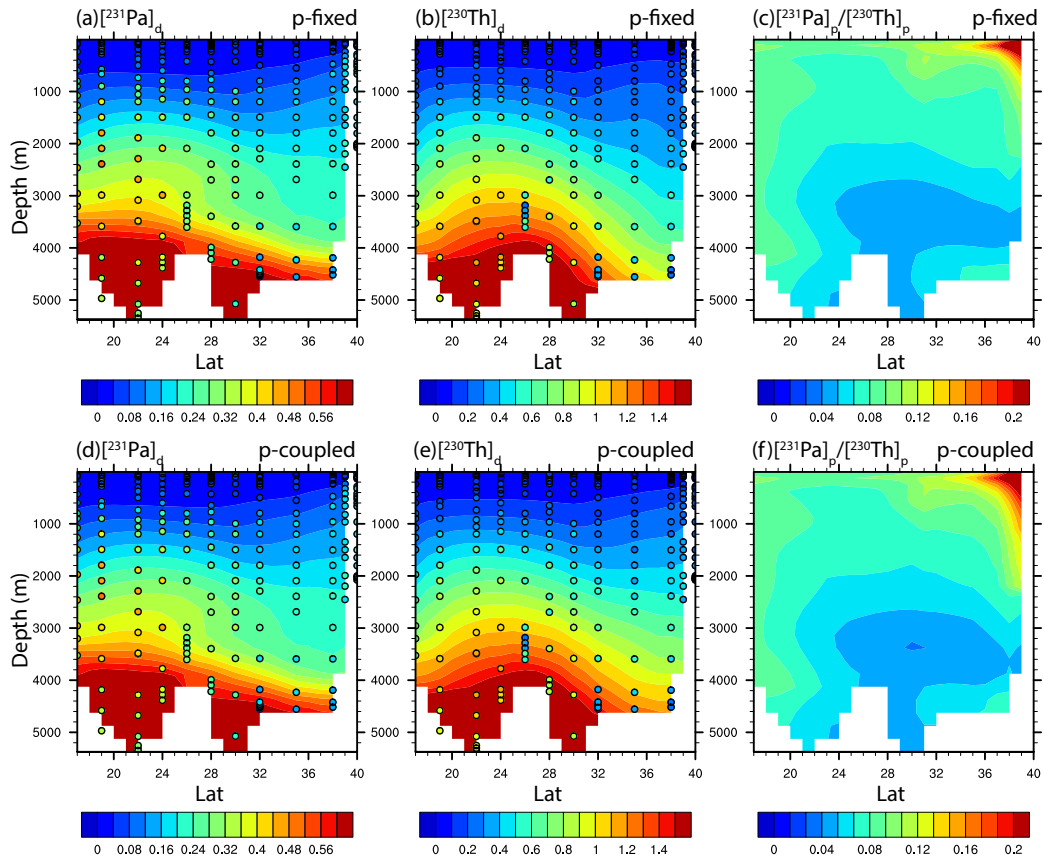


Figure 3. Dissolved  $^{231}\text{Pa}$ , dissolved  $^{230}\text{Th}$  and particulate  $^{231}\text{Pa}/^{230}\text{Th}$  in CTRL along GEOTRACES transect GA03 (Hayes et al., 2015) (the track is indicated in Fig. S4) for both p-fixed (top row) and p-coupled (bottom row)  $^{231}\text{Pa}$  and  $^{230}\text{Th}$  (colored contour). Observations of dissolved  $^{231}\text{Pa}$  and  $^{230}\text{Th}$  activity are superimposed as colored circles using the same color scale.

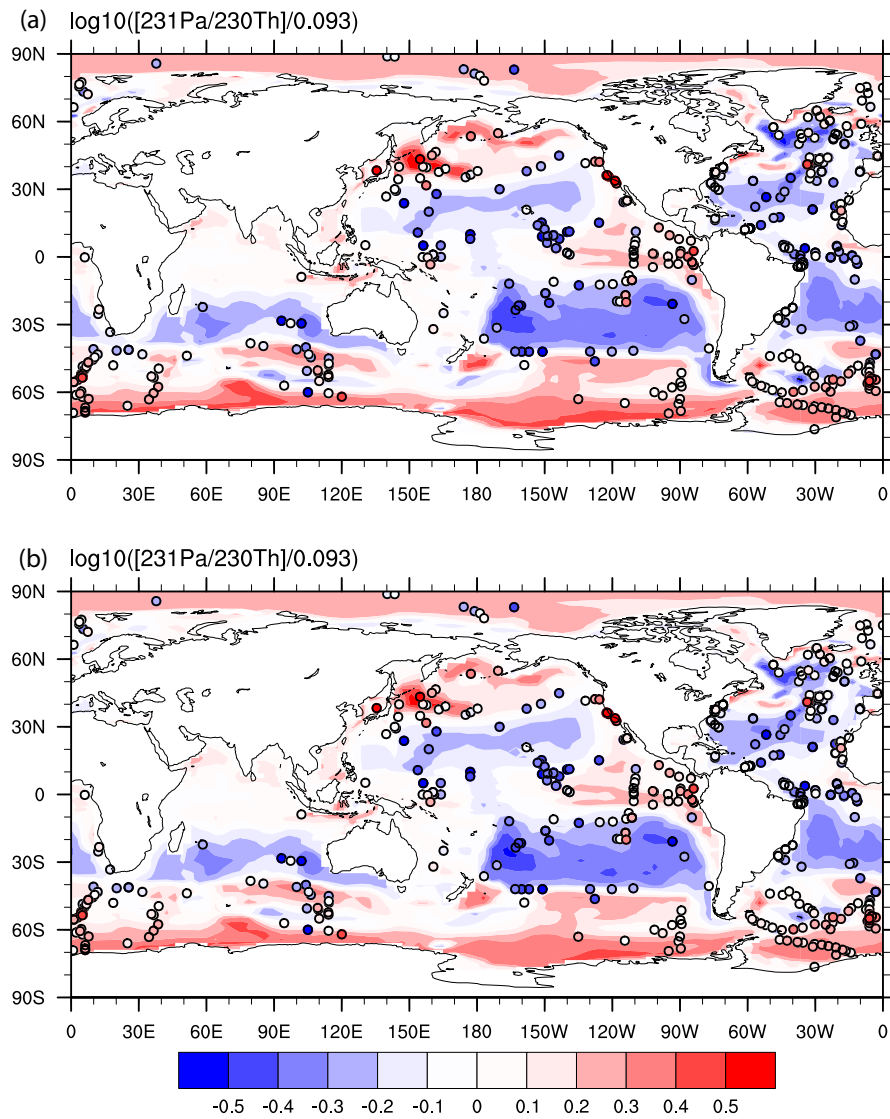
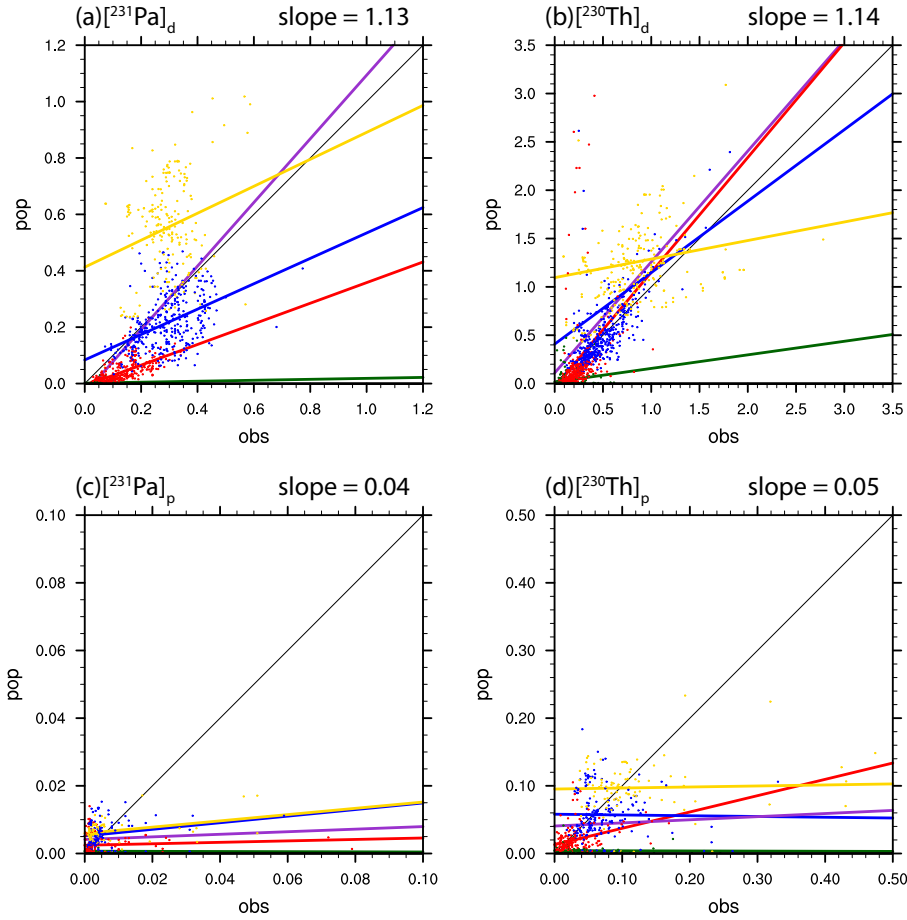


Figure 4. Sediment  $^{231}\text{Pa}/^{230}\text{Th}$  activity ratio in CTRL for both p-fixed (a) and p-coupled version (b). Observations are attached as filled cycles using the same color map. The  $^{231}\text{Pa}/^{230}\text{Th}$  activity ratio is plotted relative to the production ratio of 0.093 on a  $\log_{10}$  scale.



948

949

950 Figure 5. Scatter plot of global dissolved and particulate  $^{231}\text{Pa}$  and  $^{230}\text{Th}$  between  
 951 observation and CTRL (p-fixed) (unit: dpm/m<sup>3</sup>). (a) dissolved  $^{231}\text{Pa}$ ; (b) particulate  
 952  $^{231}\text{Pa}$ ; (c) dissolved  $^{230}\text{Th}$ ; (d) particulate  $^{230}\text{Th}$ . Observations in different depth  
 953 range are indicated by different colors: green for 0-100m; red for 100m-1,000m;  
 954 blue for 1,000m-3,000m and yellow for deeper than 3,000m. Purple line is the least  
 955 squared linear regression line for all depth range, the slope of which is indicated at  
 956 the top right of each plot. Green line is the least squared linear regression line for  
 957 depth from 0-100m. Red line is the least squared linear regression line for depth  
 958 from 100m -1,000m. Blue line is the least squared linear regression line for depth  
 959 from 1,000m-3,000m. Yellow line is the least squared linear regression line for  
 960 depth deeper than 3,000m.

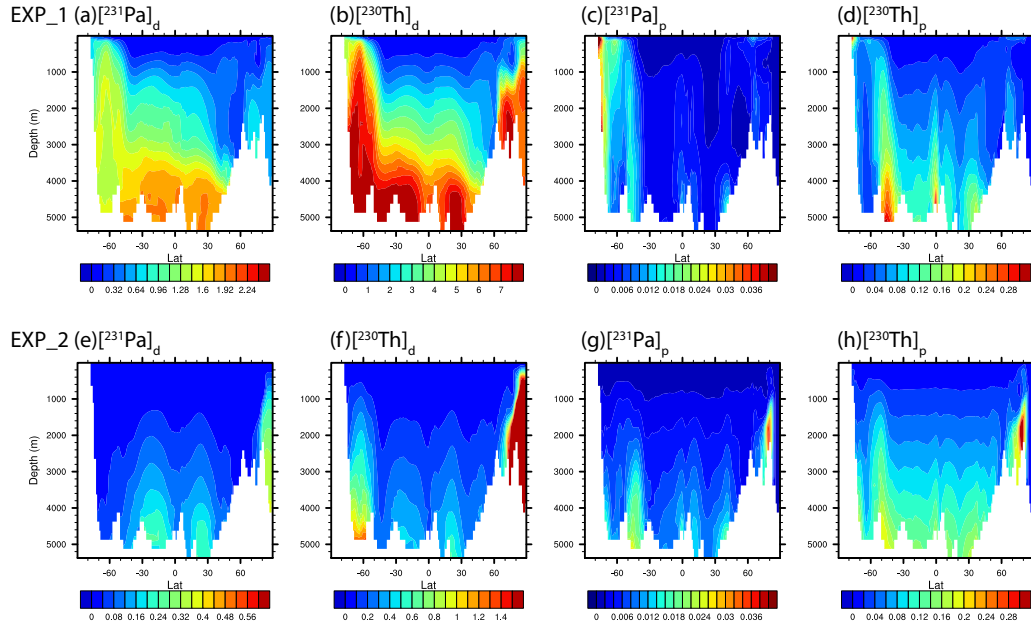


Figure 6. Atlantic zonal mean dissolved and particulate  $^{231}\text{Pa}$  and  $^{230}\text{Th}$  in EXP\_1 and EXP\_2 (unit: dpm/m<sup>3</sup>). EXP\_1: (a) dissolved  $^{231}\text{Pa}$ ; (b) dissolved  $^{230}\text{Th}$ ; (c) particulate  $^{231}\text{Pa}$ ; (d) particulate  $^{230}\text{Th}$ . EXP\_2: (e) dissolved  $^{231}\text{Pa}$ ; (f) dissolved  $^{230}\text{Th}$ ; (g) particulate  $^{231}\text{Pa}$ ; (h) particulate  $^{230}\text{Th}$ .

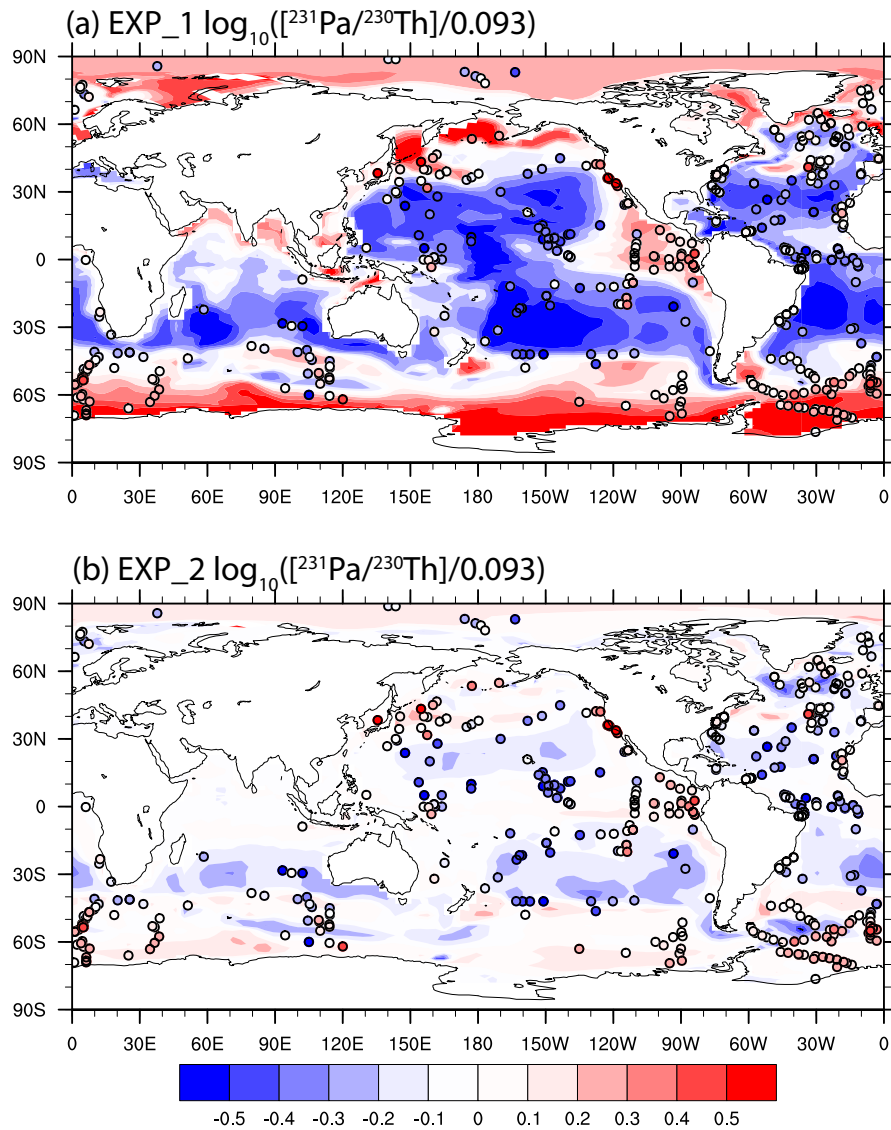


Figure 7. Sediment  $^{231}\text{Pa}/^{230}\text{Th}$  activity ratio in EXP\_1 (a) and EXP\_2 (b). Observations are attached as filled cycles using the same color map. The  $^{231}\text{Pa}/^{230}\text{Th}$  activity ratio is plotted relative to the production ratio of 0.093 on a log<sub>10</sub> scale.

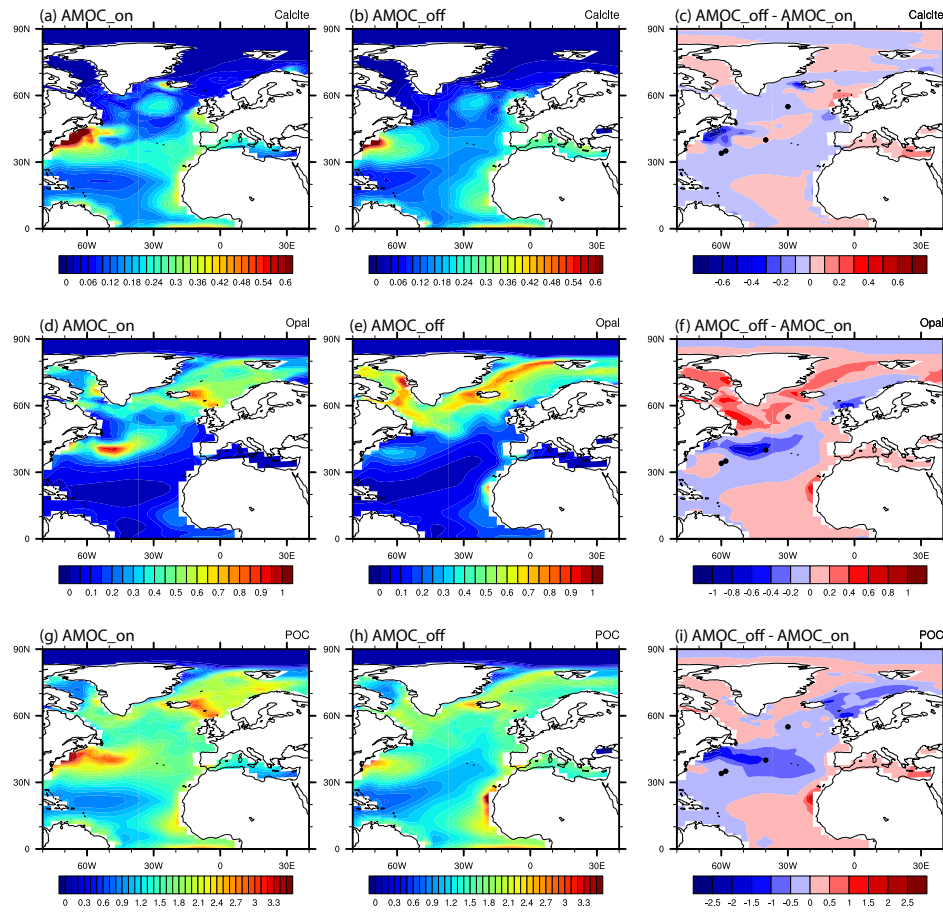
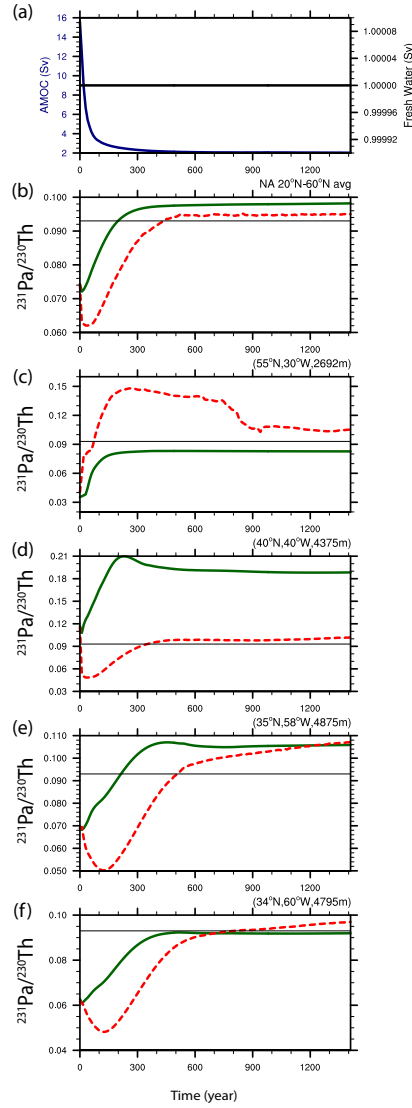


Figure 8. Comparison of particle fluxes between AMOC\_on and AMOC\_off.  $\text{CaCO}_3$  flux at 105m ( $\text{mol m}^{-2} \text{yr}^{-1}$ ) during AMOC\_on (a), AMOC\_off (b) and difference between AMOC\_off and AMOC\_on. (b) Opal flux at 105m ( $\text{mol m}^{-2} \text{yr}^{-1}$ ) during AMOC\_on (d), AMOC\_off (e) and difference between AMOC\_off and AMOC\_on (f). POC flux at 105m ( $\text{mol m}^{-2} \text{yr}^{-1}$ ) during AMOC\_on (g), AMOC\_off (h) and difference between AMOC\_off and AMOC\_on (i).



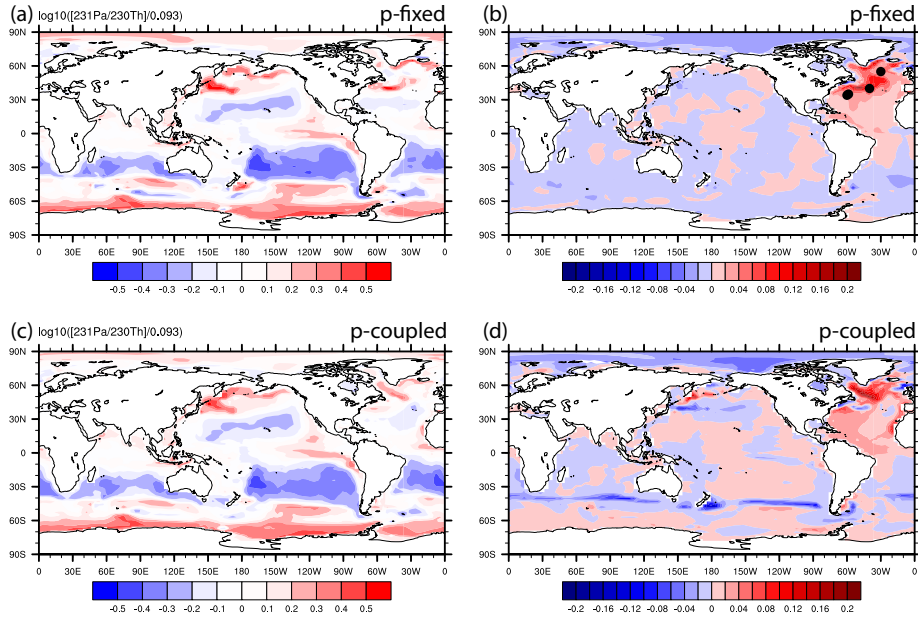


981

982

983 Figure 9. Time evolutions in HOSING. (a) Freshwater forcing (black) and AMOC  
 984 strength (navy), which is defined as the maximum of the overturning  
 985 streamfunction below 500m in the North Atlantic. (b) North Atlantic average  
 986 sediment  $^{231}\text{Pa}/^{230}\text{Th}$  activity ratio from 20°N to 60°N: p-fixed (green) and p-  
 987 coupled (red). Production ratio of 0.093 is indicated by a solid black line (similar in  
 988 c, d, e and f). (c) Sediment  $^{231}\text{Pa}/^{230}\text{Th}$  activity ratio at (55°N, 30°W). (d) Sediment  
 989  $^{231}\text{Pa}/^{230}\text{Th}$  activity ratio at (40°N, 40°W). (e) Sediment  $^{231}\text{Pa}/^{230}\text{Th}$  activity ratio at  
 990 (35°N, 58°W). (f) Sediment  $^{231}\text{Pa}/^{230}\text{Th}$  activity ratio at (34°N, 60°W). (e) and (f) are  
 991 near Bermuda Rise. Locations of each site are shown as dots in Fig. 8b.

992

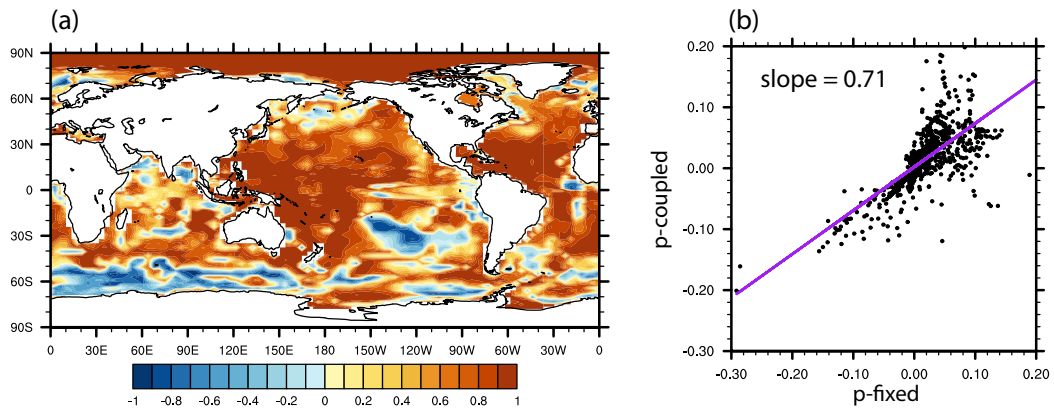


993

994

995 Figure 10. Sediment  $^{231}\text{Pa}/^{230}\text{Th}$  activity ratio during AMOC off state and the  
 996 difference between AMOC off and CTRL. (a) P-fixed  $\log_{10}([^{231}\text{Pa}/^{230}\text{Th}]/0.093)$  in  
 997 AMOC\_off. (b) Difference of p-fixed sediment  $^{231}\text{Pa}/^{230}\text{Th}$  activity ratio between  
 998 AMOC\_off and AMOC\_on. (c) and (d) are similar to (a) and (b) for p-coupled  
 999 sediment  $^{231}\text{Pa}/^{230}\text{Th}$  activity ratio. Black dots in (b) shows the locations of sites in  
 1000 Fig. 9 from North to South.

1001



1002

Figure 11. (a) Correlation of p-fixed and p-coupled evolution of sediment  $^{231}\text{Pa}/^{230}\text{Th}$  activity ratio in HOSING. (b) Scatter plot of p-fixed and p-coupled sediment  $^{231}\text{Pa}/^{230}\text{Th}$  activity ratio change from AMOC\_on to AMOC\_off in the Atlantic and the Southern Ocean (70°W-20°E). Purple line is the least squared linear regression line and slope is the linear regression coefficient.

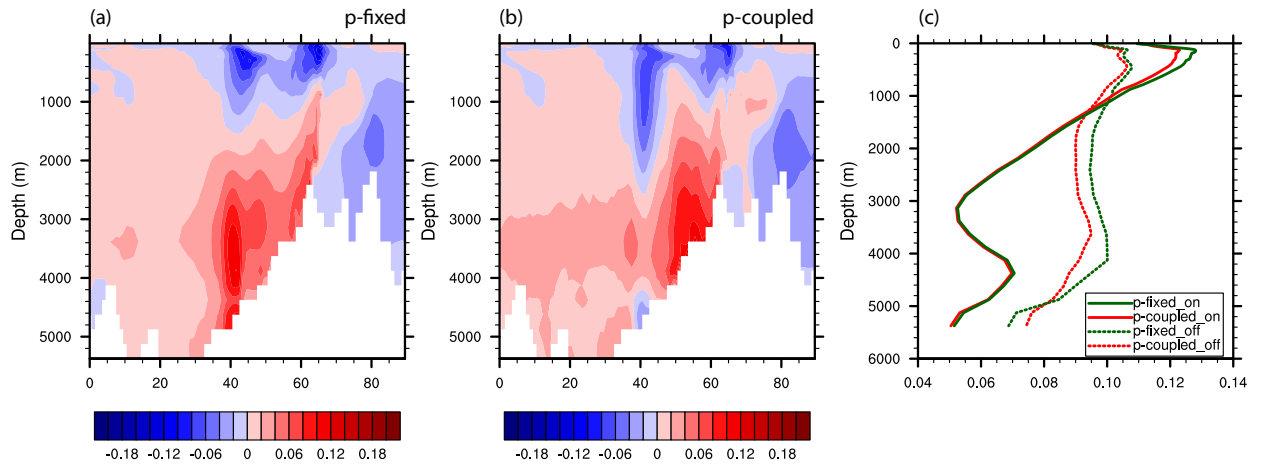


Figure 12. Difference of Atlantic zonal mean particulate  $^{231}\text{Pa}/^{230}\text{Th}$  between AMOC\_off and AMOC\_on: (a) p-fixed and (b) p-coupled. (c) North Atlantic (20°N-60°N) average profile during AMOC\_on (solid) and AMOC\_off (dash) for p-fixed (green) and p-coupled (red) particulate  $^{231}\text{Pa}/^{230}\text{Th}$ .